



# Calculation of predictions for non-identical particle correlations in heavy ions collisions at LHC energies from hydrodynamics-inspired models

MASTER OF SCIENCE THESIS

Author:  
**Mateusz Wojciech Gałażyn**

Supervisor:  
**Prof. Adam Kisiel**

Warsaw, 15th November 2014



# Wyznaczenie przewidywań teoretycznych dla korelacji cząstek nieidentycznych w zderzeniach ciężkich jonów przy energiach LHC w modelach opartych na hydrodynamice

PRACA MAGISTERSKA

Autor:  
**Mateusz Wojciech Gałażyn**

Promotor:  
**dr hab. inż. Adam Kisiel, prof. PW**

Warszawa, 15 listopada 2014

## 1 Abstract

2 This thesis presents results of two-particle momentum correlations analysis  
3 for different kinds of particles produced in heavy ion collisions. The studies  
4 were carried for the data from simulated lead-lead collisions at the centre  
5 of mass energy  $\sqrt{s_{NN}} = 2.76$  TeV in the THERMINATOR model using the  
6 (3+1)-dimensional hydrodynamic model with viscosity. Analysis was performed  
7 for the three particle kinds: pions, kaons and protons for the collisions for eight  
8 different centrality ranges.

9 The THERMINATOR model allows to perform statistical hadronization of  
10 stable particles and unstable resonances from a given hypersurface which is  
11 followed by the resonance propagation and decay phase. The four-dimensional  
12 hypersurface is coming from the calculations performed on a basis of relativistic  
13 hydrodynamic framework with the viscosity corrections.

14 One can investigate space-time characteristics of the particle-emitting source  
15 through two-particle interferometry. Through this method one can study, using  
16 the experimental observables, the properties of a system created in heavy ion  
17 collisions. The experimental-like analysis of a data coming from a model calcula-  
18 tions yields a possibility to test the hydrodynamic description of a quark-gluon  
19 plasma. This thesis concentrates on the verification of the prediction of appear-  
20 ance of femtoscopic radii scaling with the transverse mass.

21 The three dimensional correlation functions were calculated using spherical  
22 harmonics decomposition. This approach allows one to perform calculations  
23 with the less statistics and the visualization of results is much easier. The cal-  
24 culated correlation functions show expected increase of a correlation for pions  
25 and kaons at the low relative momenta of a pair. For the protons at the same mo-  
26 mentum region, the decrease occurs. The transverse pair momentum and cen-  
27 trality dependence on a correlation function is observed. In order to perform the  
28 quantitative analysis of this influence, the fitting of theoretical formula for cor-  
29 relation function was performed. The femtoscopic radii calculated in the LCMS  
30 and PRF are falling with the transverse mass  $m_T$ . To test the scaling predicted  
31 from the hydrodynamics, the power law was fitted  $\alpha m_T^{-\beta}$ . The radii calculated  
32 for pions, kaons and protons in the LCMS are following the common scaling. In  
33 case of the PRF no such scaling is observed. To recover the scaling in the PRF, the  
34 approximate factor to recover scaling is proposed:  $\sqrt{(\sqrt{\gamma_T} + 2)/3}$ . The radii in  
35 the PRF divided by the proposed scaling factor are falling on the common curve,  
36 therefore the scaling can be recovered using the proposed scaling factor. The  
37 experimental analysis is usually performed in the PRF (requires less statistics),  
38 hence the method of scaling recovery enables easier testing of the hydrodynamic  
39 predictions, which are not visible in the PRF.

## **Streszczenie**

# <sup>41</sup> Contents

<sup>42</sup>	<b>Introduction</b>	<b>1</b>
<sup>43</sup>	<b>1 Theory of heavy ion collisions</b>	<b>3</b>
<sup>44</sup>	1.1 The Standard Model . . . . .	3
<sup>45</sup>	1.2 Quantum Chromodynamics . . . . .	4
<sup>46</sup>	1.2.1 Quarks and gluons . . . . .	4
<sup>47</sup>	1.2.2 Quantum Chromodynamics potential . . . . .	5
<sup>48</sup>	1.2.3 The quark-gluon plasma . . . . .	7
<sup>49</sup>	1.3 Relativistic heavy ion collisions . . . . .	8
<sup>50</sup>	1.3.1 Stages of heavy ion collision . . . . .	8
<sup>51</sup>	1.3.2 QGP signatures . . . . .	10
<sup>52</sup>	<b>2 Therminator model</b>	<b>18</b>
<sup>53</sup>	2.1 (3+1)-dimensional viscous hydrodynamics . . . . .	18
<sup>54</sup>	2.2 Statistical hadronization . . . . .	19
<sup>55</sup>	2.2.1 Cooper-Frye formalism . . . . .	20
<sup>56</sup>	<b>3 Particle interferometry</b>	<b>22</b>
<sup>57</sup>	3.1 HBT interferometry . . . . .	22
<sup>58</sup>	3.2 Theoretical approach . . . . .	23
<sup>59</sup>	3.2.1 Conventions used . . . . .	23
<sup>60</sup>	3.2.2 Two particle wave function . . . . .	24
<sup>61</sup>	3.2.3 Source emission function . . . . .	25
<sup>62</sup>	3.2.4 Theoretical correlation function . . . . .	27
<sup>63</sup>	3.2.5 Spherical harmonics decomposition of a correlation function	28
<sup>64</sup>	3.3 Experimental approach . . . . .	29
<sup>65</sup>	3.4 Scaling of femtoscopic radii . . . . .	30
<sup>66</sup>	3.4.1 Scaling in LCMS . . . . .	31
<sup>67</sup>	3.4.2 Scaling in PRF . . . . .	31
<sup>68</sup>	<b>4 Results</b>	<b>33</b>
<sup>69</sup>	4.1 Identical particles correlations . . . . .	33
<sup>70</sup>	4.1.1 Spherical harmonics components . . . . .	33
<sup>71</sup>	4.1.2 Centrality dependence of a correlation function . . . . .	37

72	4.1.3 $k_T$ dependence of a correlation function . . . . .	38
73	4.2 Results of the fitting procedure . . . . .	39
74	4.2.1 The three-dimensional femtoscopic radii scaling . . . . .	39
75	4.2.2 Scaling of one-dimensional radii . . . . .	43
76	4.3 Discussion of the results . . . . .	44
77	<b>Conclusions</b>	<b>45</b>

# <sup>78</sup> Introduction

<sup>79</sup> Many people were trying to discover what was before the universe which we  
<sup>80</sup> observe today. Through the years there were appearing more or less successful  
<sup>81</sup> theories which were trying to describe its origin and behaviour. Among them  
<sup>82</sup> is one model, which provides a comprehensive explanation for a broad range  
<sup>83</sup> of phenomena, including the cosmic microwave background, abundance of the  
<sup>84</sup> light elements and Hubble's law. This model is called The Big Bang theory and  
<sup>85</sup> has been born in the 1927 on the basis of principles proposed by the Belgian priest and  
<sup>86</sup> scientist Georges Lemaître. Using this model and known laws of physics one can  
<sup>87</sup> calculate the characteristics of the universe in detail back in time to the extreme  
<sup>88</sup> densities and temperatures. However, at some point these calculations fail. The  
<sup>89</sup> extrapolation of the expansion of universe backwards in time using general relativity  
<sup>90</sup> yields an infinite density and temperature at a finite time in the past. This  
<sup>91</sup> appearance of singularity is a signal of the breakdown of general relativity. The  
<sup>92</sup> range of this extrapolation towards singularity is debated - certainly we can go  
<sup>93</sup> no closer than the end of *Planck epoch* i.e.  $10^{-43}$  s. At this very first era the tem-  
<sup>94</sup> perature of the universe was so high, that the four fundamental forces - electro-  
<sup>95</sup> magnetism, gravitation, weak nuclear interaction and strong nuclear interaction  
<sup>96</sup> - were one fundamental force. Between  $10^{-43}$  s and  $10^{-36}$  s of a lifetime of the  
<sup>97</sup> universe, there is a *grand unification epoch*, at which forces are starting to separate  
<sup>98</sup> from each other. From  $10^{-36}$  s to  $10^{-12}$  s lasted *electroweak epoch*, when the strong  
<sup>99</sup> force separated from the electroweak force. After the electroweak epoch, there  
<sup>100</sup> was the *quark epoch* in which the universe was a dense "soup" of quarks. During  
<sup>101</sup> this stage the fundamental forces of gravitation, electromagnetism, strong and  
<sup>102</sup> weak interactions had taken their present forms. The temperature at this mo-  
<sup>103</sup> ment was still too high to allow quarks to bind together and form hadrons. At  
<sup>104</sup> the end of quark era, there was a big freeze-out - when the average energy of  
<sup>105</sup> particle interactions had fallen below the binding energy of hadrons. This era in  
<sup>106</sup> which quarks became confined into hadrons is known as the hadron epoch. At  
<sup>107</sup> this moment the matter had started forming nuclei and atoms, which we observe  
<sup>108</sup> today.

<sup>109</sup> Here arises the question: how we can study the very beginning of the  
<sup>110</sup> universe? To do this, one should create in a laboratory a system with a such  
<sup>111</sup> large density and high temperature to recreate those conditions. Today, this is  
<sup>112</sup> achievable through sophisticated machines, which are particle accelerators. In

113 the particle accelerators, like the Large Hadron Collider at CERN, Geneva or  
114 Relativistic Heavy Ion Collider at Brookhaven National Laboratory in Upton,  
115 New York, the heavy ions after being accelerated to the near speed of light are  
116 collided in order to generate extremely dense and hot phase of matter and  
117 recreate the quark-gluon plasma. The plasma is believed to behave like an  
118 almost ideal fluid and to become a medium, that can be described by the laws of  
119 relativistic hydrodynamics.

120 This thesis is a verification of predictions for collective behaviour of the  
121 quark-gluon plasma coming from the hydrodynamic equations using the  
122 experimental-like analysis for the high energy Pb-Pb collisions generated using  
123 the THERMINATOR model.

124 The 1st chapter is an introduction to the theory of heavy ion collisions. It  
125 contains the brief description of the Standard Model and Quantum Chromody-  
126 namics. The quark-gluon plasma and its signatures are also characterized.

127 In the 2nd chapter there is a description of the relativistic hydrodynamic  
128 framework and the THERMINATOR model used to perform the simulations of col-  
129 lisions.

130 The 3rd chapter covers the particle interferometry method used in this work.  
131 The algorithm of building experimental correlation functions and effects coming  
132 from the hydrodynamics in the experimental results for particle interferometry  
133 are also presented.

134 In the 4th chapter there is a detailed analysis of the results for two-particle  
135 femtoscopy for different pairs of particles. The quantitative analysis of calcu-  
136 lated femtoscopic radii as well as the appearance of transverse mass scaling is  
137 discussed.

<sup>138</sup> **Chapter 1**

<sup>139</sup> **Theory of heavy ion collisions**

<sup>140</sup> **1.1 The Standard Model**

<sup>141</sup> In the 1970s, a new theory of fundamental particles and their interaction  
<sup>142</sup> emerged. A new concept, which concerns the electromagnetic, weak and strong  
<sup>143</sup> nuclear interactions between known particles. This theory is called *The Standard*  
<sup>144</sup> *Model*. There are seventeen named particles in the standard model, organized  
<sup>145</sup> into the chart shown below (Fig. 1.1). Fundamental particles are divided into  
two families: *fermions* and *bosons*.

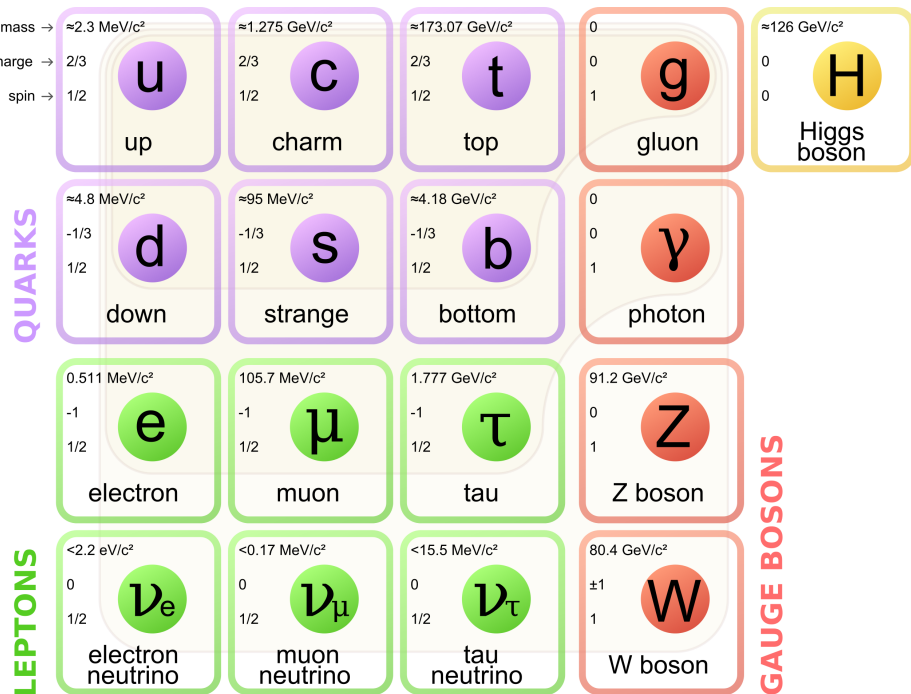


Figure 1.1: The Standard Model of elementary particles [1].

146 Fermions are the building blocks of matter. They are divided into two groups.  
 147 Six of them, which must bind together are called *quarks*. Quarks are known to  
 148 bind into doublets (*mesons*), triplets (*baryons*) and recently confirmed four-quark  
 149 states.<sup>1</sup> Two of baryons, with the longest lifetimes, are forming a nucleus: a pro-  
 150 ton and a neutron. A proton is build from two up quarks and one down, and  
 151 neutron consists of two down quarks and one up. A proton is found to be a stable  
 152 particle (at least it has a lifetime larger than  $10^{35}$  years) and a free neutron has a  
 153 mean lifetime about  $8.8 \times 10^2$  s. Fermions, that can exist independently are called  
 154 *leptons*. Neutrinos are a subgroup of leptons, which are only influenced by weak  
 155 interaction. Fermions can be divided into three generations (three columns in  
 156 the Figure 1.1). Generation I particles can combine into hadrons with the longest  
 157 life spans. Generation II and III consists of unstable particles which form also  
 158 unstable hadrons.

159 Bosons are force carriers. There are four fundamental forces: weak - respons-  
 160ible for radioactive decay, strong - coupling quarks into hadrons, electromagnetic  
 161 - between charged particles and gravity - the weakest, which causes the attraction  
 162 between particles with a mass. The Standard Model describes the first three. The  
 163 weak force is mediated by  $W^\pm$  and  $Z^0$  bosons, electromagnetic force is carried by  
 164 photons  $\gamma$  and the carriers of a strong interaction are gluons  $g$ . The fifth boson is  
 165 a Higgs boson which is responsible for giving other particles mass.

## 166 1.2 Quantum Chromodynamics

### 167 1.2.1 Quarks and gluons

168 Quarks interact with each other through the strong interaction. The mediator  
 169 of this force is a *gluon* - a massless and chargeless particle. In the quantum chro-  
 170 modynamics (QCD) - theory describing strong interaction - there are six types of  
 171 "charges" (like electrical charges in the electrodynamics) called *colours*. The col-  
 172 ours were introduced because some of the observed particles, like  $\Delta^-$ ,  $\Delta^{++}$  and  
 173  $\Omega^-$  appeared to consist of three quarks with the same flavour ( $ddd$ ,  $uuu$  and  $sss$   
 174 respectively), which was in conflict with the Pauli principle. One quark can carry  
 175 one of the three colours (usually called *red*, *green* and *blue*) and antiquark one of  
 176 the three anti-colours respectively. Only colour-neutral (or white) particles could  
 177 exist. Mesons are assumed to be a colour-anticolour pair, while baryons are *red-*  
 178 *green-blue* triplets. Gluons also are colour-charged and there are 8 types of gluons.  
 179 Therefore they can interact with themselves [3].

---

<sup>1</sup>The LHCb experiment at CERN in Geneva confirmed recently existence of  $Z(4430)$  - a particle consisting of four quarks [2].

180 **1.2.2 Quantum Chromodynamics potential**

181 As a result of that gluons are massless, one can expect, that the static potential  
 182 in the QCD will have the similar form like one in the electrodynamics e.g.  $\sim 1/r$   
 183 (through an analogy to photons). In reality the QCD potential is assumed to have  
 184 the form of [3]

$$V_s = -\frac{4}{3} \frac{\alpha_s}{r} + kr, \quad (1.1)$$

185 where the  $\alpha_s$  is a coupling constant of the strong force and the  $kr$  part is related  
 186 with the *confinement*. In comparison to the electromagnetic force, a value of the  
 187 strong coupling constant is  $\alpha_s \approx 1$  and the electromagnetic one is  $\alpha = 1/137$ .

188 The fact that quarks does not exist separately, but they are always bound,  
 189 is called a confinement. As two quarks are pulled apart, the linear part  $kr$  in  
 190 the Eq. 1.1 becomes dominant and the potential becomes proportional to the dis-  
 191 tance. This situation resembles stretching of a string. At some point, when the  
 192 string is so large it is energetically favourable to create a quark-antiquark pair. At  
 193 this moment such pair (or pairs) is formed, the string breaks and the confinement  
 is preserved (Fig. 1.2).

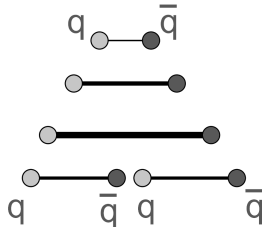


Figure 1.2: A string break and a creation of a pair quark-anti-quark [4].

194  
 195 On the other hand, for the small  $r$ , an interaction between the quarks and  
 196 gluons is dominated by the Coulomb-like term  $-\frac{4}{3} \frac{\alpha_s}{r}$ . The coupling constant  $\alpha_s$   
 197 depends on the four-momentum  $Q^2$  transferred in the interaction. This depend-  
 198 ence is presented in Fig. 1.3. The value  $\alpha_s$  decreases with increasing momentum  
 199 transfer and the interaction becomes weak for large  $Q^2$ , i.e.  $\alpha_s(Q) \rightarrow 0$ . Be-  
 200 cause of weakening of coupling constant, quarks at large energies (or small dis-  
 201 tances) are starting to behave like free particles. This phenomenon is known as  
 202 an *asymptotic freedom*. The QCD potential has also temperature dependence - the  
 203 force strength “melts” with the temperature increase. Therefore the asymptotic  
 204 freedom is expected to appear in either the case of high baryon densities (small  
 205 distances between quarks) or very high temperatures. This temperature depend-  
 206 ence is illustrated in the Fig. 1.4.

207 If the coupling constant  $\alpha_s$  is small, one can use perturbative methods to cal-  
 208 culate physical observables. Perturbative QCD (pQCD) successfully describes  
 209 hard processes (with large  $Q^2$ ), such as jet production in high energy proton-  
 210 antiproton collisions. The applicability of pQCD is defined by the *scale parameter*

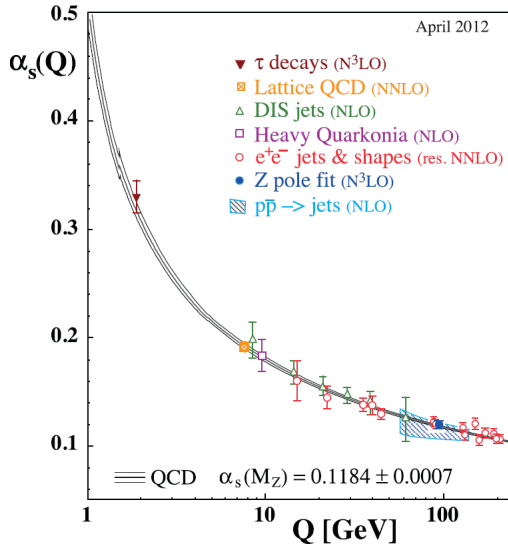


Figure 1.3: The coupling parameter  $\alpha_s$  dependence on four-momentum transfer  $Q^2$  [5].

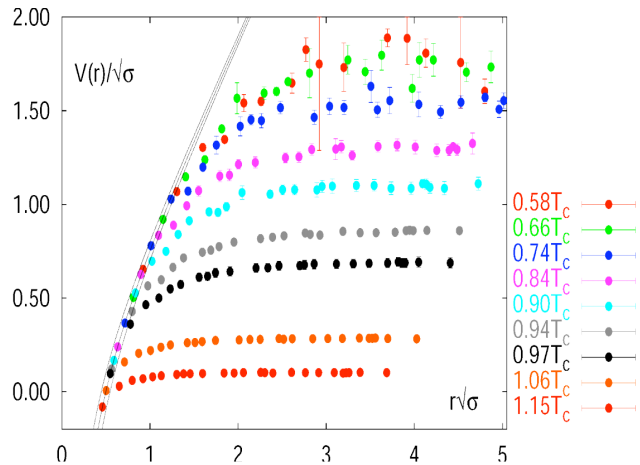


Figure 1.4: The QCD potential for a pair quark-antiquark as a function of distance for different temperatures. A value of a potential decreases with the temperature [4].

211  $\Lambda_{QCD} \approx 200$  MeV. If  $Q \gg \Lambda_{QCD}$  then the process is in the perturbative domain  
212 and can be described by pQCD. A description of soft processes (when  $Q < 1$  GeV)  
213 is a problem in QCD - perturbative theory breaks down at this scale. Therefore,  
214 to describe processes with low  $Q^2$ , one has to use alternative methods like Lattice  
215 QCD. Lattice QCD (LQCD) is non-perturbative implementation of a field theory  
216 in which QCD quantities are calculated on a discrete space-time grid. LQCD al-

lows to obtain properties of matter in equilibrium, but there are some limitations. Lattice QCD requires fine lattice spacing to obtain precise results - therefore large computational resources are necessary. With the constant growth of computing power this problem will become less important. The second problem is that lattice simulations are possible only for baryon density  $\mu_B = 0$ . At  $\mu_B \neq 0$ , Lattice QCD breaks down because of the sign problem [6].

### 1.2.3 The quark-gluon plasma

The new state of matter in which quarks are no longer confined is known as a *quark-gluon plasma* (QGP). The predictions coming from the discrete space-time Lattice QCD calculations reveal a phase transition from the hadronic matter to the quark-gluon plasma at the high temperatures and baryon densities. The res-

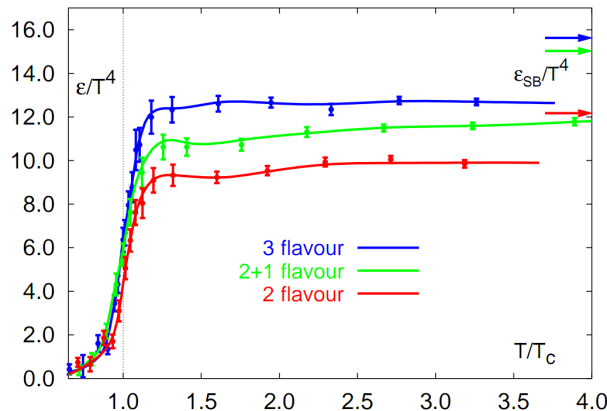


Figure 1.5: A number of degrees of freedom as a function of a temperature [7].

ults obtained from such calculations are shown on Fig. 1.5. The energy density  $\epsilon$  which is divided by  $T^4$  is a measure of number of degrees of freedom in the system. One can observe significant rise of this value, when the temperature increases past the critical value  $T_C$ . Such increase is signaling a phase transition - the formation of QGP [8]. The values of the energy densities plotted in Fig. 1.5 do not reach the Stefan-Boltzmann limit  $\epsilon_{SB}$  (marked with arrows), which corresponds to an ideal gas. This can indicate some residual interactions in the system. According to the results from the RHIC<sup>2</sup>, the new phase of matter behaves more like an ideal fluid, than like a gas [9].

One of the key questions, to which current heavy ion physics tries to find an answer is the value of a critical temperature  $T_C$  as a function of a baryon chemical potential  $\mu_B$  (baryon density), where the phase transition occur. The results coming from the Lattice QCD are presented in the Fig. 1.6. The phase of matter in which quarks and gluons are deconfined is expected to exist at large

<sup>2</sup>Relativistic Heavy Ion Collider at Brookhaven National Laboratory in Upton, New York

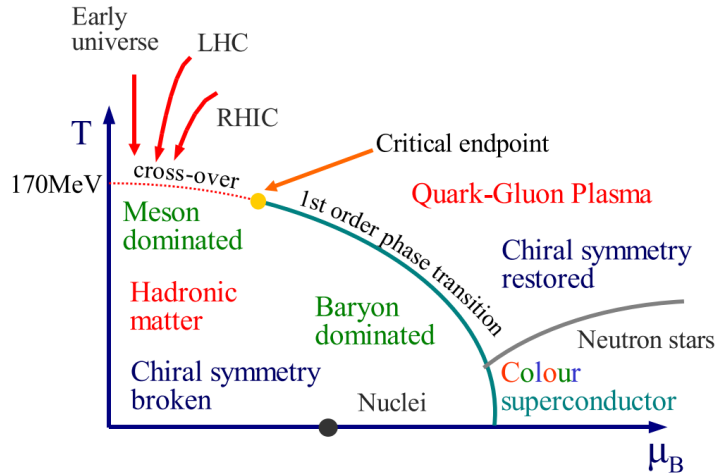


Figure 1.6: Phase diagram coming from the Lattice QCD calculations [8].

temperatures. In the region of small temperatures and high baryon densities, a different state is supposed to appear - a *colour superconductor*. The phase transition between hadronic matter and QGP is thought to be of 1<sup>st</sup> order at  $\mu_B \gg 0$ . However as  $\mu_B \rightarrow 0$  quarks' masses become significant and a sharp transition transforms into a rapid but smooth cross-over. It is believed that in Pb-Pb collisions observed at the LHC<sup>3</sup>, the created matter has high enough temperature to be in the quark-gluon plasma phase, then cools down and converts into hadrons, undergoing a smooth transition [8].

### 1.3 Relativistic heavy ion collisions

#### 1.3.1 Stages of heavy ion collision

To create the quark-gluon plasma one has to achieve high enough temperatures and baryon densities. Such conditions can be recreated in the heavy ion collisions at the high energies. The left side of the Figure 1.7 shows simplified picture of a central collision of two highly relativistic nuclei in the centre-of-mass reference frame. The colliding nuclei are presented as thin disks because of the Lorentz contraction. In the central region, where the energy density is the highest, a new state of matter - the quark-gluon plasma - is supposedly created. Afterwards, the plasma expands ad cools down, quarks combine into hadrons and their mutual interactions cease when the system reaches the *freeze-out* temperature. Subsequently, produced free hadrons move towards the detectors.

On the right side of the Figure 1.7 there is presented a space-time evolution of a collision process, plotted in the light-cone variables ( $z, t$ ). The two highly

<sup>3</sup>Large Hadron Collider at CERN, Geneva

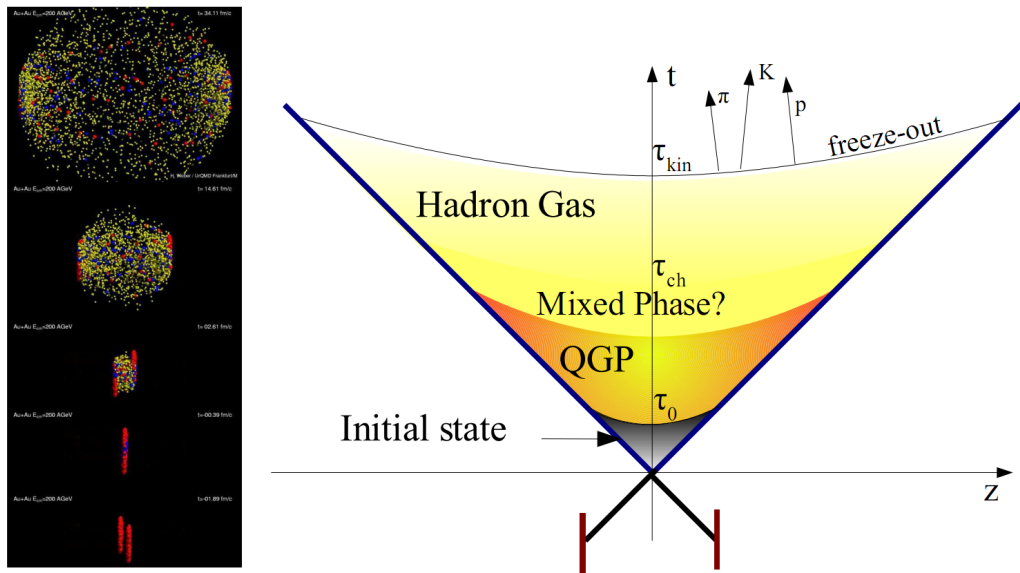


Figure 1.7: Left: stages of a heavy ion collision simulated in the UrQMD model. Right: schematic view of a heavy ion collision evolution [8].

264 relativistic nuclei are traveling basically along the light cone until they collide  
 265 at the centre of diagram. Nuclear fragments emerge from the collision again  
 266 along the (forward) light cone, while the matter between fragmentation zones  
 267 populates the central region. This hot and dense matter is believed to be in the  
 268 state of the quark-gluon plasma. There exist several frameworks to describe this  
 269 transition to the QGP phase, for example: QCD string breaking, QCD parton cas-  
 270 cades or colour glass condensate evolving into glasma and later into quark-gluon  
 271 plasma [10].

272 **String breaking** – In the string picture, the nuclei pass through each other forming  
 273 colour strings. This is analogous to the situation depicted in the Fig 1.2 - the  
 274 colour string is created between quarks inside particular nucleons in nuclei. In  
 275 the next step strings decay / fragment forming quarks and gluons or directly  
 276 hadrons. This approach becomes invalid at very high energies, when the strings  
 277 overlap and cannot be treated as independent objects.

278 **Parton cascade** – The parton<sup>4</sup> cascade model is based on the pQCD. The col-  
 279 liding nuclei are treated as clouds of quarks and which penetrate through each  
 280 other. The key element of this method is the time evolution of the parton phase-  
 281 space distributions, which is governed by a relativistic Boltzmann equation with  
 282 a collision term that contains dominant perturbative QCD interations. The bot-  
 283 tleneck of the parton cascade model is the low energies regime, where the  $Q^2$  is  
 284 too small to be described by the perturbative theory.

<sup>4</sup>A parton is a common name for a quark and a gluon.

285 **Colour glass condensate** – The colour glass condensate assumes, that the hadron can be viewed as a tightly packed system of interacting gluons. The saturation of gluons increases with energy, hence the total number of gluons may increase without the bound. Such a saturated and weakly coupled gluon system  
 286 is called a colour glass condensate. The fast gluons in the condensate are Lorentz  
 287 contracted and redistributed on the two very thin sheets representing two col-  
 288 liding nuclei. The sheets are perpendicular to the beam axis. The fast gluons  
 289 produce mutually orthogonal colour magnetic and electric fields, that only ex-  
 290 ist on the sheets. Immediately after the collision, i.e. just after the passage of  
 291 the two gluonic sheets after each other, the longitudinal electric and magnetic  
 292 fields are produced forming the *glasma*. The glasma fields decay through the  
 293 classical rearrangement of the fields into radiation of gluons. Also decays due to  
 294 the quantum pair creations are possible. In this way, the quark-gluon plasma is  
 295 produced.  
 296

297 Interactions within the created quark-gluon plasma bring the system into the  
 298 local statistical equilibrium, hence its further evolution can be described by the  
 299 relativistic hydrodynamics. The hydrodynamic expansion causes that the sys-  
 300 tem becomes more and more dilute. The phase transition from the quark-gluon  
 301 plasma to the hadronic gas occurs. Further expansion causes a transition from the  
 302 strongly interaction hadronic gas to weakly interacting system of hadrons which  
 303 move freely to the detectors. Such decoupling of hadrons is called the *freeze-out*.  
 304 The freeze-out can be divided into two phases: the chemical freeze-out and the  
 305 thermal one. The *chemical freeze-out* occurs when the inelastic collisions between  
 306 constituents of the hadron gas stop. As the system evolves from the chemical  
 307 freeze-out to the thermal freeze-out the dominant processes are elastic collisions  
 308 (such as, for example  $\pi + \pi \rightarrow \rho \rightarrow \pi + \pi$ ) and strong decays of heavier res-  
 309 onances which populate the yield of stable hadrons. The *thermal freeze-out* is the  
 310 stage of the evolution of matter, when the strongly coupled system transforms  
 311 to a weakly coupled one (consisting of essentially free particles). In other words  
 312 this is the moment, where the hadrons practically stop to interact. Obviously, the  
 313 temperatures corresponding to the two freeze-outs satisfy the condition  
 314

$$T_{chem} > T_{therm}, \quad (1.2)$$

315 where  $T_{chem}$  (inferred from the ratios of hadron multiplicities) is the temperature  
 316 of the chemical freeze-out, and  $T_{therm}$  (obtained from the investigation of the  
 317 transverse-momentum spectra) is the temperature of the thermal freeze-out [10].  
 318

### 319 1.3.2 QGP signatures

320 The quark-gluon plasma is a very short living and unstable state of matter.  
 321 One cannot investigate the properties of a plasma and confirm its existence di-  
 322 rectly. Hence, the several experimental effects were proposed as QGP signatures,  
 323 some of them have been already observed in heavy ion experiments [8]. As mat-  
 324 ter created in the heavy ions collisions is supposed to behave like a fluid, one

should expect appearance of collective behaviour at small transverse momenta - so called *elliptic flow* and *radial flow*. The next signal is the temperature range obtained from the measurements of *direct photons*, which gives us information, that the system created in heavy ion collisions is far above the critical temperature obtained from the LQCD calculations. The *puzzle in the di-lepton spectrum* can be explained by the modification of spectral shape of vector mesons (mostly  $\rho$  meson) in the presence of a dense medium. This presence of a medium can also shed light on the *jet quenching* phenomenon - the suppression occurrence in the high  $p_T$  domain.

### Elliptic flow

In a non-central heavy ion collisions, created region of matter has an almond shape with its shorter axis in the *reaction plane* (Fig. 1.8). The pressure gradient is much larger in-plane rather than out-of-plane. This causes larger acceleration and transverse velocities in-plane rather than out-of-plane. Such differences can

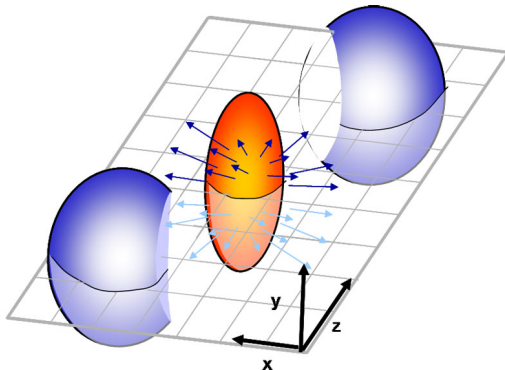


Figure 1.8: Overlapping region which is created in heavy ion collisions has an almond shape. Visible x-z plane is a *reaction plane*. The x-y plane is a *transverse plane*. The z is a direction of the beam [11].

be investigated by studying the distribution of particles with respect to the reaction plane orientation [12]:

$$E \frac{d^3 N}{dp^3} = \frac{1}{2\pi} \frac{d^2 N}{p_T dp_T dy} (1 + 2v_1 \cos(\phi) + 2v_2 \cos(2\phi) + \dots), \quad (1.3)$$

where  $\phi$  is the angle between particle transverse momentum  $p_T$  (a momentum projection on a transverse plane) and the reaction plane,  $N$  is a number of particles and  $E$  is an energy of a particle. The  $y$  variable is a *rapidity* defined as:

$$y = \frac{1}{2} \ln \left( \frac{E + p_L}{E - p_L} \right), \quad (1.4)$$

344 where  $p_L$  is a longitudinal component of a momentum (parallel to the beam direction).  
 345 The  $v_n$  coefficients indicate the shape of a system. For the most central collisions  
 346 ( $b = 0$  - see Fig. 1.9) all coefficients vanish  $\sum_{n \in N_+} v_n = 0$  (the overlapping region has the spherical shape). The Fourier series elements in the parentheses

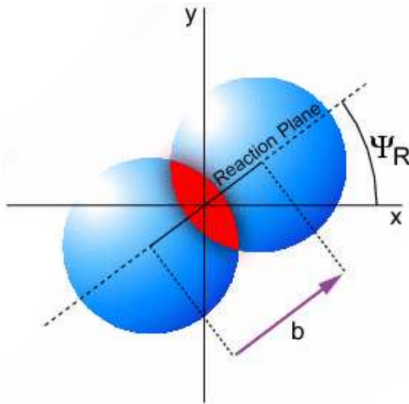


Figure 1.9: Cross-section of a heavy ion collision in a transverse plane.  $\Psi_R$  is an angle between transverse plane and the reaction plane. The  $b$  parameter is an *impact parameter* - a distance between centers of nuclei during a collision. An impact parameter is related with the centrality of a collision and a volume of the quark-gluon plasma [12].

347 in Eq. 1.3 represent different kinds of a flow. The first value: "1" represents the  
 348 *radial flow* - an isotropic flow in every direction. Next coefficient  $v_1$  is responsible  
 349 for *direct flow*. The  $v_2$  coefficient is a measure of elliptic anisotropy (*elliptic flow*).  
 350 The  $v_2$  has to build up in the early stage of a collision - later the system becomes  
 351 too dilute: space asymmetry and the pressure gradient vanish. Therefore the  
 352 observation of elliptic flow means that the created matter was in fact a strongly  
 353 interacting matter.

354 The  $v_2$  coefficient was measured already at CERN SPS, LHC and RHIC. For  
 355 the first time hydrodynamics successfully described the collision dynamics as the  
 356 measured  $v_2$  reached hydrodynamic limit (Fig. 1.10). As expected, there is a mass  
 357 ordering of  $v_2$  as a function of  $p_T$  (lower plot in the Fig. 1.10) with pions having  
 358 the largest and protons the smallest anisotropy. In the upper plots in the Fig. 1.10  
 359 there is a  $v_2$  as a function of transverse kinetic energy. The left plot shows the  
 360 two universal trend lines for baryons and mesons. After the scaling of  $v_2$  and the  
 361 kinetic energy by the number of valence quarks, all of the hadrons follow the  
 362 same universal curve. Those plots show that strong collectivity is observed in  
 363 heavy ion collisions.

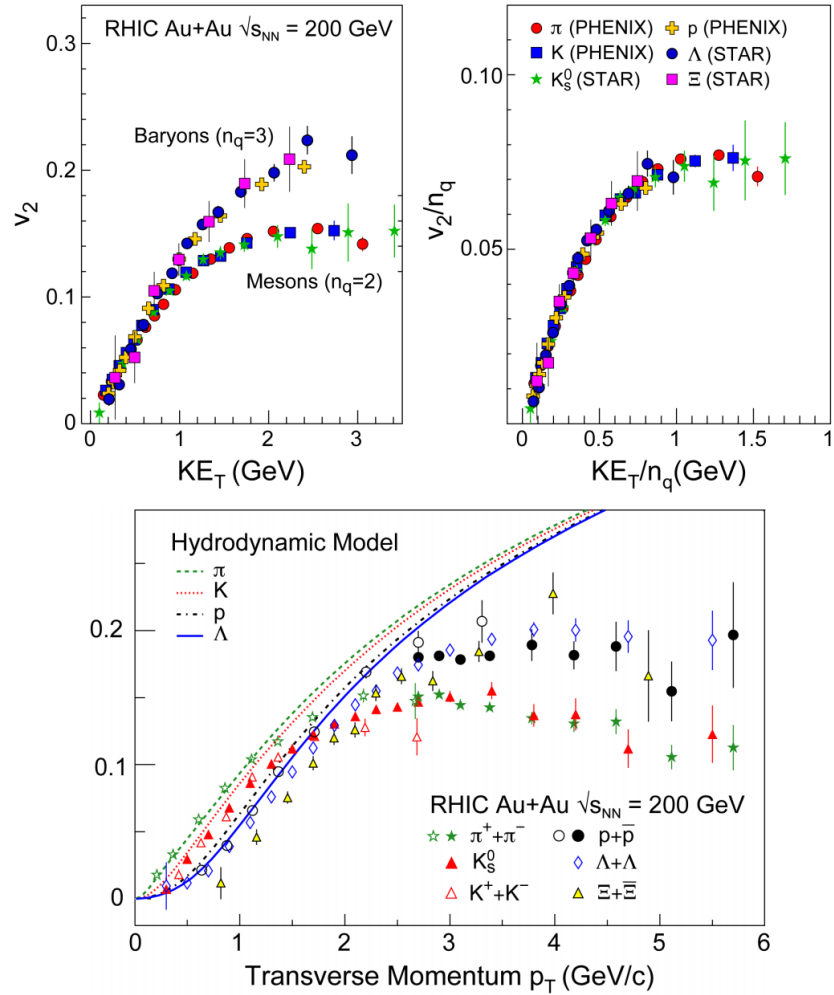


Figure 1.10: *Lower:* The elliptic flow  $v_2$  follows the hydrodynamical predictions for an ideal fluid perfectly. Note that > 99% of all final hadrons have  $p_T < 1.5$  GeV/c. *Upper left:* The  $v_2$  plotted versus transverse kinetic energy  $KE_T = m_T - m_0 = \sqrt{p_T^2 + m_0^2} - m_0$ . The  $v_2$  follows different universal curves for mesons and baryons. *Upper right:* When scaled by the number of valence quarks, the  $v_2$  follows the same universal curve for all hadrons and for all values of scaled transverse kinetic energy [13].

### 365    Transverse radial flow

366    Elliptic flow described previously is caused by the pressure gradients which  
 367    must also produce a more simple collective behaviour of matter - a movement  
 368    inside-out, called radial flow. Particles are pushed to higher momenta and they  
 369    move away from the center of the collision. A source not showing collective

370 behaviour, like pp collisions, produces particle spectra that can be fitted by a  
 371 power-law [8]:

$$\frac{1}{2\pi p_T} \frac{d^2N}{dp_T d\eta} = C \left( 1 + \frac{p_T}{p_0} \right)^{-\gamma}. \quad (1.5)$$

372 The  $\eta$  variable is a *pseudorapidity* defined as follows:

$$\eta = \frac{1}{2} \ln \left( \frac{p + p_L}{p - p_L} \right) = -\ln \left( \frac{\theta}{2} \right), \quad (1.6)$$

where  $\theta$  is an emission angle  $\cos \theta = p_L/p$ .

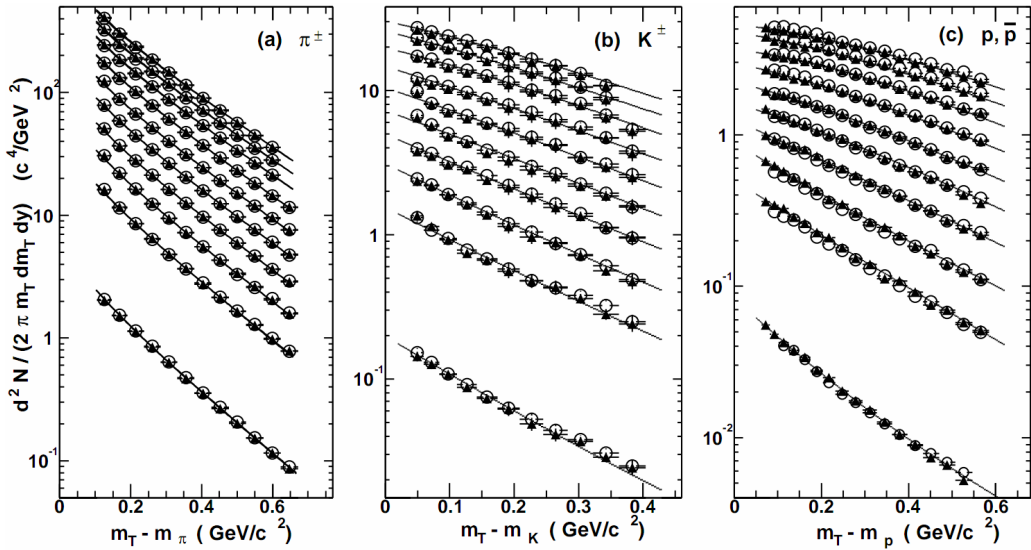


Figure 1.11: Invariant yield of particles versus transverse mass  $m_T = \sqrt{p_T^2 + m_0^2}$  for  $\pi^\pm$ ,  $K^\pm$ ,  $p$  and  $\bar{p}$  at mid-rapidity for p+p collisions (bottom) and Au+Au events from 70-80% (second bottom) to 0-5% (top) centrality [14].

373  
 374 The hydrodynamical expansion of a system gives the same flow velocity kick  
 375 for different kind of particles - ones with bigger masses will gain larger  $p_T$  boost.  
 376 This causes increase of the yield of particles with larger transverse momenta. In  
 377 the invariant yield plots one can observe the decrease of the slope parameter,  
 378 especially for the heavier hadrons. This is presented in the Fig. 1.11. The most  
 379 affected spectra are ones of kaons (b) and protons (c). One can notice decrease  
 380 of the slope parameter for heavy ion collisions (plots from second bottom to top)  
 381 comparing to the proton-proton collisions (bottom ones), where no boost from  
 382 radial flow should occur [8].

### 383 Direct photons

384 The direct photons are photons, which are not coming from the final state  
 385 hadrons decays. Their sources can be various interaction from charged particles

created in the collision, either at the partonic or at the hadronic level. Direct photons are considered to be an excellent probe of the early stage of the collision. This is because their mean free path is very large to the created system in the collision. Thus photons created at the early stage leave the system without suffering any interaction and retain information about this stage, in particular about its temperature.

One can distinguish two kinds of direct photons: *thermal* and *prompt*. Thermal photons can be emitted from the strong processes in the quark-gluon plasma involving quarks and gluons or hot hadronic matter (e.g. processes:  $\pi\pi \rightarrow \rho\gamma$ ,  $\pi\rho \rightarrow \pi\gamma$ ). Thermal photons can be observed in the low  $p_T$  region. Prompt photons are believed to come from “hard” collisions of initial state partons belonging to the colliding nuclei. The prompt photons can be described using the pQCD. They will dominate the high  $p_T$  region. The analysis of transverse momentum of spectra of direct photons revealed, that the temperature of the source of thermal photons produced in heavy ion collisions at RHIC is in the range 300-600 MeV (Fig. 1.12). Hence the direct photons had to come from a system whose temperature is far above from the critical temperature for QGP creation.

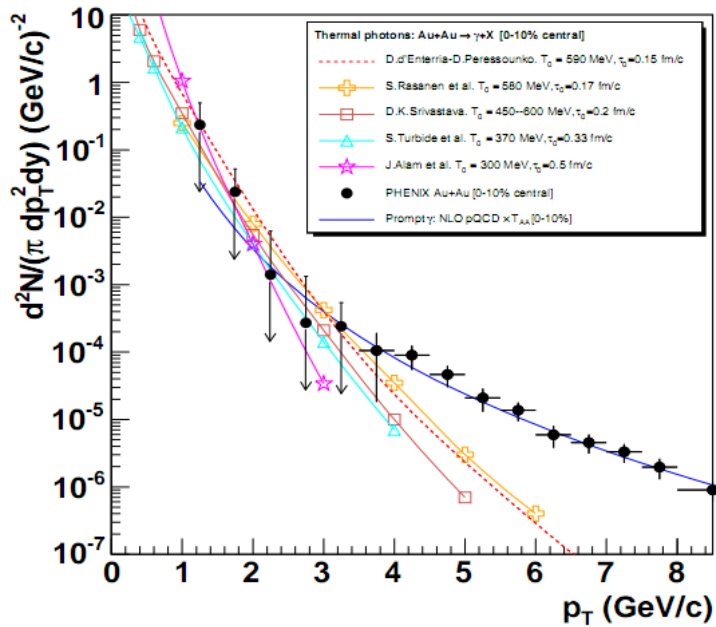


Figure 1.12: Thermal photons spectra for the central Au+Au collisions at  $\sqrt{s_{NN}} = 200$  GeV computed within different hydrodynamical models compared with the pQCD calculations (solid line) and experimental data from PHENIX (black dots) [15].

403 **Puzzle in di-lepton mass spectrum**

404 The invariant mass spectra (Fig. 1.13) of lepton pairs reveal many peaks cor-  
 405 responding to direct decays of various mesons into a lepton pair. The continu-  
 406 ous background in this plot is caused by the decays of hadrons into more than  
 407 two leptons (including so-called *Dalitz decays* into a lepton pair and a photon).  
 Particular hadron decay channels, which contribute to this spectrum are shown

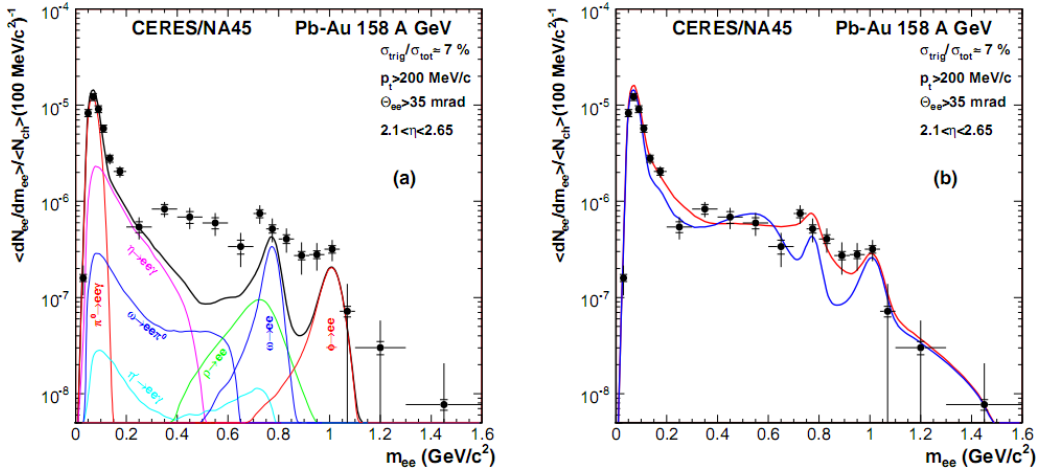


Figure 1.13: Left: Invariant mass spectrum of  $e^+ - e^-$  pairs in  $\text{Pb} + \text{Au}$  collisions at 158A GeV compared to the sum coming from the hadron decays predictions. Right: The expectations coming from model calculations assuming a dropping of the  $\rho$  mass (blue) or a spread of the  $\rho$  width in the medium (red) [16].

408 in the Fig. 1.13 with the coloured lines and their sum with the black one. The  
 409 sum (called *the hadronic cocktail*) of various components describes experimen-  
 410 tal spectra coming from the simple collisions (like  $p + p$  or  $p + A$ ) quite well with the  
 411 statistical and systematical uncertainties [9]. This situation is different consider-  
 412 ing more complicated systems i.e.  $A + A$ . Spectra coming from  $\text{Pb} + \text{Au}$  collisions  
 413 are presented on the plots in the Fig. 1.13. The “hadronic cocktail” does not de-  
 414 scribe the data, in the mass range between the  $\pi$  and the  $\rho$  mesons a significant  
 415 excess of electron pairs over the calculated sum is observed. Theoretical expla-  
 416 nation of this phenomenon assumes modification of the spectral shape of vector  
 417 mesons in a dense medium. Two different interpretations of this increase were  
 418 proposed: a decrease of meson mass with the medium density and increase of the  
 419 meson width in the dense medium. In principle, one could think of simultaneous  
 420 occurrence of both effects: mass shift and resonance broadening. Experimental  
 421 results coming from the CERES disfavour the mass shift hypothesis indicating  
 422 only broadening of resonance peaks (Fig. 1.13b) [9].

424 **Jet quenching**

425 A jet is defined as a group of particles with close vector momenta and high en-  
 426 ergies. It has its beginning when the two partons are going in opposite directions  
 427 and have energy big enough to produce new quark-antiquark pair and then ra-  
 428 diate gluons. This process can be repeated many times and it results in two back-  
 429 to-back jets of hadrons. It has been found that jets in the opposite hemisphere  
 430 (*away-side jets*) show a very different pattern in d+Au and Au+Au collisions. This  
 431 is shown in the azimuthal correlations in the Fig. 1.14. In d+Au collisions, like in  
 432 p+p, a pronounced away-side jet appears around  $\Delta\phi = \pi$ , exactly opposite to the  
 433 trigger jet, what is typical for di-jet events. In central Au+Au collisions the away-  
 jet is suppressed. When the jet has its beginning near the surface of the quark-

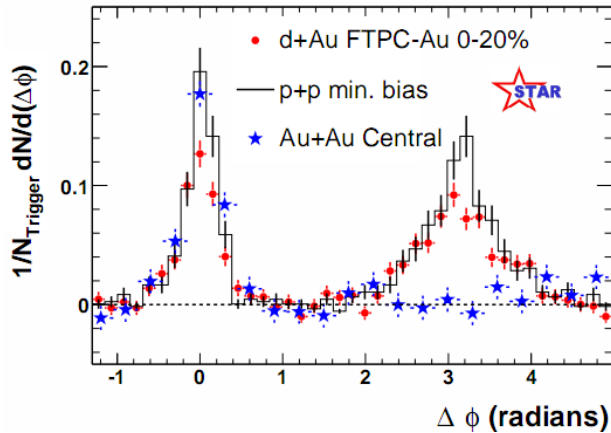


Figure 1.14: Azimuthal angle difference  $\Delta\phi$  distributions for different colliding systems at  $\sqrt{s_{NN}} = 200$  GeV. Transverse momentum cut:  $p_T > 2$  GeV. For the Au+Au collisions the away-side jet is missing [17].

434  
 435 gluon plasma, one of the jets (*near-side jet*) leaves the system almost without any  
 436 interactions. This jet is visible on the correlation plot as a high peak at  $\Delta\phi = 0$ .  
 437 However, the jet moving towards the opposite direction has to penetrate a dense  
 438 medium. The interaction with the plasma causes energy dissipation of particles  
 439 and is visible on an azimuthal correlation plot as disappearance of the away-side  
 440 jet [9].

441 **Chapter 2**

442 **Therminator model**

443 THERMINATOR [18] is a Monte Carlo event generator designed to investigate  
444 the particle production in the relativistic heavy ion collisions. The functionality  
445 of the code includes a generation of the stable particles and unstable resonances  
446 at the chosen hypersurface model. It performs the statistical hadronization which  
447 is followed by space-time evolution of particles and the decay of resonances. The  
448 key element of this method is an inclusion of a complete list of hadronic reso-  
449 nances, which contribute very significantly to the observables. The second version  
450 of THERMINATOR [19] comes with a possibility to incorporate any shape of freeze-  
451 out hypersurface and the expansion velocity field, especially those generated ex-  
452 ternally with various hydrodynamic codes.

453 **2.1 (3+1)-dimensional viscous hydrodynamics**

454 Most of the relativistic viscous hydrodynamic calculations are done in  
455 (2+1)-dimensions. Such simplification assumes boost-invariance of a matter  
456 created in a collision. Experimental data reveals that no boost-invariant region is  
457 formed in the collisions [20]. Hence, for the better description of created system  
458 a (3+1)-dimensional model is required.

459 In the four dimensional relativistic dynamics one can describe a system  
460 using a space-time four-vector  $x^\nu = (ct, x, y, z)$ , a velocity four-vector  
461  $u^\nu = \gamma(c, v_x, v_y, v_z)$  and a energy-momentum tensor  $T^{\mu\nu}$ . The particular  
462 components of  $T^{\mu\nu}$  have a following meaning:

- 463 •  $T^{00}$  - an energy density,
- 464 •  $cT^{0\alpha}$  - an energy flux across a surface  $x^\alpha$ ,
- 465 •  $T^{\alpha 0}$  - an  $\alpha$ -momentum flux across a surface  $x^\alpha$  multiplied by  $c$ ,
- 466 •  $T^{\alpha\beta}$  - components of momentum flux density tensor,

467 where  $\gamma = (1 - v^2/c^2)^{-1/2}$  is Lorentz factor and  $\alpha, \beta \in \{1, 2, 3\}$ . Using  $u^\nu$  one can  
468 express  $T^{\mu\nu}$  as follows [21]:

$$T_0^{\mu\nu} = (e + p)u^\mu u^\nu - pg^{\mu\nu} \quad (2.1)$$

469 where  $e$  is an energy density,  $p$  is a pressure and  $g^{\mu\nu}$  is an inverse metric tensor:

$$g^{\mu\nu} = \begin{bmatrix} 1 & 0 & 0 & 0 \\ 0 & -1 & 0 & 0 \\ 0 & 0 & -1 & 0 \\ 0 & 0 & 0 & -1 \end{bmatrix}. \quad (2.2)$$

470 The presented version of energy-momentum tensor (Eq. 2.1) can be used to de-  
471 scribe dynamics of a perfect fluid. To take into account influence of viscosity,  
472 one has to apply the following corrections coming from shear  $\pi^{\mu\nu}$  and bulk  $\Pi$   
473 viscosities [22]:

$$T^{\mu\nu} = T_0^{\mu\nu} + \pi^{\mu\nu} + \Pi(g^{\mu\nu} - u^\mu u^\nu). \quad (2.3)$$

474 The stress tensor  $\pi^{\mu\nu}$  and the bulk viscosity  $\Pi$  are solutions of dynamical equa-  
475 tions in the second order viscous hydrodynamic framework [21]. The compari-  
476 son of hydrodynamics calculations with the experimental results reveal, that the  
477 shear viscosity divided by entropy  $\eta/s$  has to be small and close to the AdS/CFT  
478 estimate  $\eta/s = 0.08$  [22, 23]. The bulk viscosity over entropy value used in calcu-  
479 lations is  $\zeta/s = 0.04$  [22].

480 When using  $T^{\mu\nu}$  to describe system evolving close to local thermodynamic  
481 equilibrium, relativistic hydrodynamic equations in a form of:

$$\partial_\mu T^{\mu\nu} = 0 \quad (2.4)$$

482 can be used to describe the dynamics of the local energy density, pressure and  
483 flow velocity.

484 Hydrodynamic calculations are starting from the Glauber<sup>1</sup> model initial con-  
485 ditions. The collective expansion of a fluid ends at the freeze-out hypersurface.  
486 That surface is usually defined as a constant temperature surface, or equivalently  
487 as a cut-off in local energy density. The freeze-out is assumed to occur at the  
488 temperature  $T = 140$  MeV.

## 489 2.2 Statistical hadronization

490 Statistical description of heavy ion collision has been successfully used  
491 to describe quantitatively *soft* physics, i.e. the regime with the transverse  
492 momentum not exceeding 2 GeV. The basic assumption of the statistical  
493 approach of evolution of the quark-gluon plasma is that at some point of the

---

<sup>1</sup>The Glauber Model is used to calculate “geometrical” parameters of a collision like an impact parameter, number of participating nucleons or number of binary collisions.

space-time evolution of the fireball, the thermal equilibrium is reached. When the system is in the thermal equilibrium the local phase-space densities of particles follow the Fermi-Dirac or Bose-Einstein statistical distributions. At the end of the plasma expansion, the freeze-out occurs. The freeze-out model incorporated in the THERMINATOR model assumes, that chemical and thermal freeze-out occur at the same time.

### 2.2.1 Cooper-Frye formalism

The result of the hydrodynamic calculations is the freeze-out hypersurface  $\Sigma^\mu$ . A three-dimensional element of the surface is defined as [19]

$$d\Sigma_\mu = \epsilon_{\mu\alpha\beta\gamma} \frac{\partial x^\alpha}{\partial \alpha} \frac{\partial x^\beta}{\partial \beta} \frac{\partial x^\gamma}{\partial \gamma} d\alpha d\beta d\gamma, \quad (2.5)$$

where  $\epsilon_{\mu\alpha\beta\gamma}$  is the Levi-Civita tensor and the variables  $\alpha, \beta, \gamma \in \{1, 2, 3\}$  are used to parametrize the three-dimensional freeze-out hypersurface in the Minkowski four-dimensional space. The Levi-Civita tensor is equal to 1 when the indices form an even permutation (eg.  $\epsilon_{0123}$ ), to -1 when the permutation is odd (e.g.  $\epsilon_{2134}$ ) and has a value of 0 if any index is repeated. Therefore [19],

$$d\Sigma_0 = \begin{vmatrix} \frac{\partial x}{\partial \alpha} & \frac{\partial x}{\partial \beta} & \frac{\partial x}{\partial \gamma} \\ \frac{\partial y}{\partial \alpha} & \frac{\partial y}{\partial \beta} & \frac{\partial y}{\partial \gamma} \\ \frac{\partial z}{\partial \alpha} & \frac{\partial z}{\partial \beta} & \frac{\partial z}{\partial \gamma} \end{vmatrix} d\alpha d\beta d\gamma \quad (2.6)$$

and the remaining components are obtained by cyclic permutations of  $t, x, y$  and  $z$ .

One can obtain the number of hadrons produced on the hypersurface  $\Sigma^\mu$  from the Cooper-Frye formalism. The following integral yields the total number of created particles [19]:

$$N = (2s + 1) \int \frac{d^3 p}{(2\pi)^3 E_p} \int d\Sigma_\mu p^\mu f(p_\mu u^\mu), \quad (2.7)$$

where  $f(p_\mu u^\mu)$  is the phase-space distribution of particles (for stable ones and resonances). One can simply derive from Eq. 2.7, the dependence of the momentum density [24]:

$$E \frac{d^3 N}{dp^3} = \int d\Sigma_\mu f(p_\mu u^\mu) p^\mu. \quad (2.8)$$

The momentum distribution  $f$  contains non-equilibrium corrections:

$$f = f_0 + \delta f_{shear} + \delta f_{bulk}, \quad (2.9)$$

where

$$f_0(p_\mu u^\mu) = \left\{ \exp \left[ \frac{p_\mu u^\mu - (B\mu_B + I_3\mu_{I_3} + S\mu_S + C\mu_C)}{T} \right] \pm 1 \right\}^{-1} \quad (2.10)$$

519 In case of fermions, in the Eq. 2.10 there is a plus sign and for bosons, minus  
 520 sign respectively. The thermodynamic quantities appearing in the  $f_0(\cdot)$  are  $T$  -  
 521 temperature,  $\mu_B$  - baryon chemical potential,  $\mu_{I_3}$  - isospin chemical potential,  $\mu_S$   
 522 - strange chemical potential,  $\mu_C$  - charmed chemical potential and the  $s$  is a spin of  
 523 a particle. The hydrodynamic calculations yield the flow velocity at freeze-out as  
 524 well as the stress and bulk viscosity tensors required to calculate non-equilibrium  
 525 corrections to the momentum distribution used in Eq. 2.7. The term coming from  
 526 shear viscosity has a form [22]

$$\delta f_{shear} = f_0(1 \pm f_0) \frac{1}{2T^2(e + p)} p^\mu p^\nu \pi_{\mu\nu} \quad (2.11)$$

527 and bulk viscosity

$$\delta f_{bulk} = C f_0(1 \pm f_0) \left( \frac{(u^\mu p_\mu)^2}{3u^\mu p_\mu} - c_s^2 u^\mu p_\mu \right) \Pi \quad (2.12)$$

528 where  $c_s$  is sound velocity and

$$\frac{1}{C} = \frac{1}{3} \frac{1}{(2\pi)^3} \sum_{hadrons} \int d^3p \frac{m^2}{E} f_0(1 \pm f_0) \left( \frac{p^2}{3E} - c_s^2 E \right). \quad (2.13)$$

529 The equations presented above are directly used in the THERMINATOR to gen-  
 530 erate the primordial hadrons (created during freeze-out) with the Monte-Carlo  
 531 method. Resonances produced in this way, propagate and decay, in cascades if  
 532 necessary. For every generated particle, its origin point either on a hypersurface  
 533 or is associated with the point of the decay of the parent particle. This informa-  
 534 tion is kept in the simulation due to its importance for the femtoscopic analysis.

535 **Chapter 3**

536 **Particle interferometry**

537 Two-particle interferometry (also called *femtoscopy*) gives a possibility to  
538 investigate space-time characteristics of the particle-emitting source created  
539 in heavy ion collisions. Through the study of particle correlations, their  
540 momentum distributions can be used to obtain information about the spatial  
541 extent of the created system. Using this method, one can measure sizes of the  
542 order of  $10^{-15}$  m and time of the order of  $10^{-23}$  s.

543 **3.1 HBT interferometry**

544 In the 1956 Robert Hanbury Brown and Richard Q. Twiss proposed a  
545 method which through analysis of interference between photons allowed to  
546 investigate angular dimensions of stars. The most important result from the  
547 Hanbury-Brown-Twiss experiments is that two indistinguishable particles can  
548 produce an interference effect. There is almost no difference between normal  
549 interferometry and HBT method, except that the latter one does not take into account  
550 information about phase shift of registered particles. At the beginning  
551 this method was used in astronomy for photon interference, but this effect can  
552 be used also to measure extent of any emitting source. This method was adapted  
553 to heavy ion collisions to investigate dimensions of a system created in those  
554 collisions by studying correlations of identical particles [25]. The main difference  
555 between HBT method in astronomy and femtoscopy is that the first one is based  
556 on space-time HBT correlations and the latter one uses momentum correlations.  
557 The momentum correlations yield the space-time picture of the source, whereas  
558 the space-time HBT correlations provide the characteristic relative momenta of  
559 emitted photons, which gives the angular size of the star without the knowledge  
560 of its radius and lifetime [10].

561 **3.2 Theoretical approach**

562 Intensity interferometry in heavy ion physics uses similar mathematical form-  
 563 alism as the astronomy HBT measurement. Through the measurement of corre-  
 564 lation between particles as a function of their relative momentum one can deduce  
 565 the average separation between emitting sources.

566 **3.2.1 Conventions used**

567 In heavy ion collisions to describe particular directions, components of mo-  
 568 mentum and location of particles, one uses naming convention called the Bertsch-  
 569 Pratt coordinate system. This system is presented in the Fig. 3.1. The three dir-

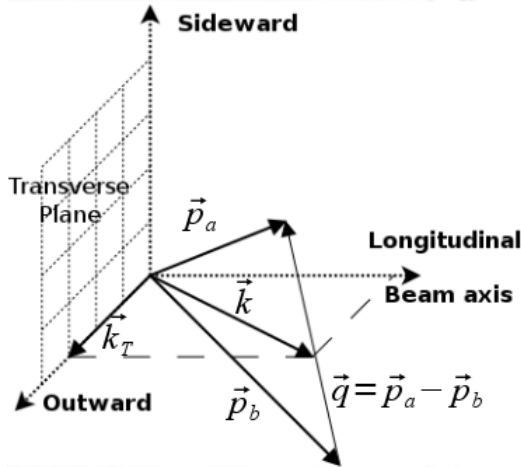


Figure 3.1: Bertsch-Pratt direction naming convention used in heavy ion collision.

569 ections are called *longitudinal*, *outward* and *sideward*. The longitudinal direction  
 570 is parallel to the beam axis. The plane perpendicular to the beam axis is called  
 571 a *transverse plane*. A projection of a particle pair momentum  $\mathbf{k} = (\mathbf{p}_a + \mathbf{p}_b)/2$   
 572 on a transverse plane (a *transverse momentum*  $\mathbf{k}_T$ ) determines *outward* direction:  
 573  $(\mathbf{k})_{out} = \mathbf{k}_T$ . A direction perpendicular to the longitudinal and outward is called  
 574 *sideward*.

575 A particle pair is usually described using two coordinate systems. The first  
 576 one, *Longitudinally Co-Moving System* (**LCMS**) is moving along the particle pair  
 577 with the longitudinal direction, in other words, the pair longitudinal momentum  
 578 vanishes:  $(\mathbf{p}_a)_{long} = -(\mathbf{p}_b)_{long}$ . The second system is called *Pair Rest Frame* (**PRF**).  
 579 In the PRF the centre of mass rests:  $\mathbf{p}_a = -\mathbf{p}_b$ . Variables which are expressed in  
 580 the PRF are marked with a star (e.g.  $\mathbf{k}^*$ ).

581 The transition of space-time coordinates from LCMS to PRF is simply  
 582 a boost along the outward direction, with the transverse velocity of the

pair  $\beta_T = (\mathbf{v}/c)_{out}$  [25]:

$$r_{out}^* = \gamma_t(r_{out} - \beta_T \Delta t) \quad (3.1)$$

$$r_{side}^* = r_{side} \quad (3.2)$$

$$r_{long}^* = r_{long} \quad (3.3)$$

$$\Delta t^* = \gamma_T(\Delta t - \beta_T r_{out}) , \quad (3.4)$$

where  $\gamma_T = (1 - \beta_T^2)^{-1/2}$  is the Lorentz factor. However, in calculations performed in this work the equal time approximation is used, which assumes that particles in a pair were produced at the same time in PRF - the  $\Delta t^*$  is neglected.

The most important variables used to describe particle pair are their total momentum  $\mathbf{P} = \mathbf{p}_a + \mathbf{p}_b$  and relative momentum  $\mathbf{q} = \mathbf{p}_a - \mathbf{p}_b$ . In the PRF one has  $\mathbf{q} = 2\mathbf{k}^*$ , where  $\mathbf{k}^*$  is a momentum of the first particle in PRF.

### 3.2.2 Two particle wave function

Let us consider two identical particles with momenta  $\mathbf{p}_1$  and  $\mathbf{p}_2$  emitted from space points  $\mathbf{x}_1$  and  $\mathbf{x}_2$ . Those emitted particles can be treated as two incoherent waves. If the particles are identical, they are also indistinguishable, therefore one

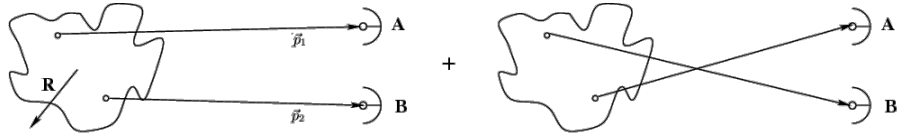


Figure 3.2: The pair wave function is a superposition of all possible states. In case of particle interferometry it includes two cases: particles with momenta  $p_1, p_2$  registered by detectors  $A, B$  and  $p_1, p_2$  registered by  $B, A$  respectively.

has also take into account the scenario, where the particle with momentum  $\mathbf{p}_1$  is emitted from  $\mathbf{x}_2$  and particle  $\mathbf{p}_2$  from  $\mathbf{x}_1$  (Fig. 3.2). In such case, the wave function describing behaviour of a pair has to contain both components [8]:

$$\Psi_{ab}(\mathbf{q}) = \frac{1}{\sqrt{2}} [\exp(-i\mathbf{p}_1\mathbf{x}_1 - i\mathbf{p}_2\mathbf{x}_2) \pm \exp(-i\mathbf{p}_2\mathbf{x}_1 - i\mathbf{p}_1\mathbf{x}_2)] . \quad (3.5)$$

A two particle wave function of identical bosons is symmetric ("+" sign in Eq. 3.5) and in case of identical fermions - antisymmetric ("−" sign). This anti-symmetrization or symmetrization implies the correlation effect coming from the Fermi-Dirac or Bose-Einstein statistics accordingly.

To provide full description of a system consisting of two charged hadrons, one has to include in the wave function besides quantum statistics also Coulomb and strong Final State Interactions. Considering identical particles systems, the quantum statistics is a main source of a correlation. Hence, in case of space-time analysis of particle emitting source, effects coming from the Coulomb and Strong interactions can be neglected.

605 **3.2.3 Source emission function**

606 To describe particle emitting source, one uses a single emission function [25]:

$$607 \quad S_A(\mathbf{x}_1, \mathbf{p}_1) = \int S(\mathbf{x}_1, \mathbf{p}_1, \mathbf{x}_2, \mathbf{p}_2, \dots, \mathbf{x}_N, \mathbf{p}_N) d\mathbf{x}_2 d\mathbf{p}_2 \dots d\mathbf{x}_N d\mathbf{p}_N \quad (3.6)$$

608 and a two-particle one:

$$S_{AB}(\mathbf{x}_1, \mathbf{p}_1, \mathbf{x}_2, \mathbf{p}_2) = \int S(\mathbf{x}_1, \mathbf{p}_1, \mathbf{x}_2, \mathbf{p}_2, \dots, \mathbf{x}_N, \mathbf{p}_N) d\mathbf{x}_3 d\mathbf{p}_3 \dots d\mathbf{x}_N d\mathbf{p}_N . \quad (3.7)$$

609 Emission function  $S(\cdot)$  can be interpreted as a probability to emit a particle, or  
 610 a pair of particles from a given space-time point with a given momentum. In  
 611 principle, the source emission function should encode all physics aspects of the  
 612 particle emission process i.e. the symmetrization for bosons and fermions, as  
 613 well as the two-body and many body Final State Interactions. Instead of this,  
 614 one assume that each particle's emission process is independent - the interac-  
 615 tion between final-state particles after their creation is independent from their  
 616 emission process. The assumption of this independence allows to construct two-  
 617 particle emission function from single particle emission functions via a convolu-  
 618 tion [25]:

$$S(\mathbf{k}^*, \mathbf{r}^*) = \int S_A(\mathbf{p}_1, \mathbf{x}_1) S_B(\mathbf{p}_2, \mathbf{x}_2) \delta \left[ \mathbf{k}^* - \frac{\mathbf{p}_1 + \mathbf{p}_2}{2} \right] \delta [\mathbf{r}^* - (\mathbf{x}_1 + \mathbf{x}_2)] \times d^4 \mathbf{x}_1 d^4 \mathbf{x}_2 d^4 \mathbf{x}_1 d^3 \mathbf{p}_1 d^3 \mathbf{p}_2 \quad (3.8)$$

619 In case of identical particles, ( $S_A = S_B$ ) several simplifications can be made.  
 620 A convolution of the two same Gaussian distributions is also a Gaussian distri-  
 621 bution with  $\sigma$  multiplied by  $\sqrt{2}$ . Femtoscopy can give information only about  
 622 two-particle emission function, but when considering Gaussian distribution as  
 623 a source function in Eq. 3.8, one can obtain a  $\sigma$  of a single emission function  
 624 from a two-particle emission function. The Eq. 3.8 is not reversible - an inform-  
 625 ation about  $S_A(\cdot)$  cannot be derived from  $S_{AB}(\cdot)$ . An exception from this rule  
 626 is a Gaussian source function, hence it is often used in femtoscopic calculations.  
 627 Considering pairs of identical particles, an emission function is assumed to be  
 628 described by the following equation in the Pair Rest Frame [25]:

$$S_{1D}^{PRF}(\mathbf{r}^*) = \exp \left( -\frac{r_{out}^{*2} + r_{side}^{*2} + r_{long}^{*2}}{4R_{inv}^2} \right) . \quad (3.9)$$

To change from the three-dimensional variables to the one-dimensional variable  
 one requires introduction of the proper Jacobian  $r^{*2}$ .

$$S_{1D}^{PRF}(r^*) = r^{*2} \exp \left( -\frac{r^{*2}}{4R_{inv}^2} \right) . \quad (3.10)$$

629 The “4” in the denominator before the “standard deviation”  $R_{inv}$  in the Gaussian  
 630 distribution comes from the convolution of the two Gaussian distributions,  
 631 which multiplies the  $R_{inv}$  by a factor of  $\sqrt{2}$ .

A more complex form of emission function was used by all RHIC and SPS experiments in identical pion femtoscopy:

$$S_{3D}^{LCMS}(\mathbf{r}) = \exp \left( -\frac{r_{out}^2}{4R_{out}^2} - \frac{r_{side}^2}{4R_{side}^2} - \frac{r_{long}^2}{4R_{long}^2} \right). \quad (3.11)$$

632 The main difference of this source function is that it has three different and inde-  
 633 pendent widths  $R_{out}$ ,  $R_{side}$ ,  $R_{long}$  and they are defined in the LCMS, not in PRF.  
 634 Unlike in PRF, in LCMS an equal-time approximation is not used. For identical  
 635 particles this is not a problem - only Coulomb interaction inside a wave function  
 636 depends on  $\Delta t$ .

### 637 Relationship between one-dimensional and three-dimensional source sizes

638 Up to now, most of femtoscopic measurements were limited only to averaged  
 639 source size  $R_{av}^L$  (the letter “L” in superscript stands for LCMS):

$$S_{1D}^{LCMS}(\mathbf{r}) = \exp \left( -\frac{r_{out}^2 + r_{side}^2 + r_{long}^2}{2R_{av}^L} \right). \quad (3.12)$$

640 The relationship between between  $S_{1D}^{LCMS}(\cdot)$  and  $S_{3D}^{LCMS}(\cdot)$  is given by:

$$S_{3D}^{LCMS}(r) = \int \exp \left( -\frac{r_{out}^2}{2R_{out}^L} - \frac{r_{side}^2}{2R_{side}^L} - \frac{r_{long}^2}{2R_{long}^L} \right) \times \delta \left( r - \sqrt{r_{out}^2 + r_{side}^2 + r_{long}^2} \right) dr_{out} dr_{side} dr_{long}. \quad (3.13)$$

641 The one-dimensional source size corresponding to the three-dimensional one can  
 642 be approximated by the following form:

$$S_{1D}^{LCMS}(r) = r^2 \exp \left( -\frac{r^2}{2R_{av}^L} \right). \quad (3.14)$$

643 The equation above assumes that  $R_{out}^L = R_{side}^L = R_{long}^L$  hence  $R_{av}^L = R_{out}^L$ . If this  
 644 condition is not satisfied, one can not give explicit mathematical relation between  
 645 one-dimensional and three-dimensional source sizes. However, for realistic val-  
 646 ues of  $R$  (i.e. for similar values of  $R_{out}$ ,  $R_{side}$ ,  $R_{long}$ ), the  $S_{3D}^{LCMS}$  from Eq. 3.13 is  
 647 not very different from Gaussian distribution and can be well approximated by  
 648 Eq. 3.13.

649 A deformation of an averaged source function in case of big differences in  
 650  $R_{out}$ ,  $R_{side}$ ,  $R_{long}$  is presented in the Fig. 3.3. A three-dimensional Gaussian dis-  
 651 tribution with varying widths was averaged into one-dimensional function using

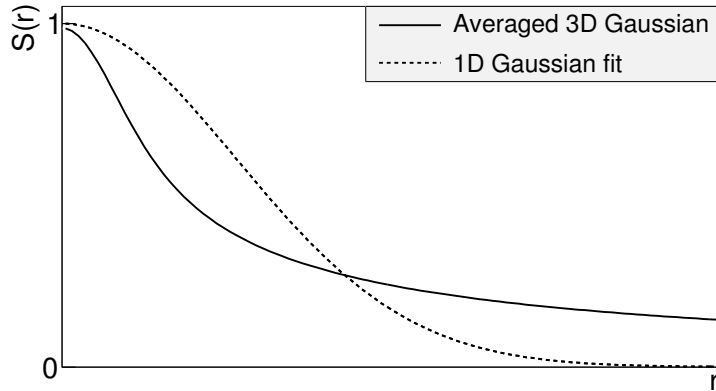


Figure 3.3: An averaged three-dimensional Gaussian source function with different widths was averaged into one-dimensional function. To illustrate deformations, one-dimensional Gaussian distribution was fitted.

the Eq. 3.13. Afterwards, an one-dimensional Gaussian distribution was fitted.  
One can notice a heavy tail of an averaged distribution in long  $r$  region, which  
makes an approximation using one-dimensional distribution in this case quite  
inaccurate.

Using Eq. 3.13 and Eq. 3.14 one can obtain a relation between one-dimensional width and the three-dimensional ones. Through numerical calculations one can find the following approximate relation [25]:

$$R_{av}^L = \sqrt{\left(R_{out}^{L^2} + R_{side}^{L^2} + R_{long}^{L^2}\right)/3}. \quad (3.15)$$

This equation does not depend on the pair velocity, hence it is valid in the LCMS and PRF.

### 3.2.4 Theoretical correlation function

The fundamental object in a particle interferometry is a correlation function.  
The correlation function is defined as:

$$C(\mathbf{p}_a, \mathbf{p}_b) = \frac{P_2(\mathbf{p}_a, \mathbf{p}_b)}{P_1(\mathbf{p}_a)P_1(\mathbf{p}_b)}, \quad (3.16)$$

where  $P_2$  is a conditional probability to observe a particle with momentum  $\mathbf{p}_b$  if particle with momentum  $\mathbf{p}_a$  was also observed. A  $P_1$  is a probability to observe a particle with a given momentum. The relationship between source emission function, pair wave function and the correlation function is described by the following equation:

$$C(\mathbf{p}_1, \mathbf{p}_2) = \int S_{AB}(\mathbf{p}_1, \mathbf{x}_1, \mathbf{p}_2, \mathbf{x}_2) |\Psi_{AB}|^2 d^4\mathbf{x}_1 d^4\mathbf{x}_2 \quad (3.17)$$

Substituting the one-dimensional emission function (Eq. 3.10) into the integral above yields the following form of correlation function in PRF:

$$C(q) = 1 + \lambda \exp(-R_{inv}^2 q^2) \quad (3.18)$$

where  $q$  is a momentum difference between two particles. When using the three-dimensional emission function (Eq. 3.11) one gets the following correlation function defined in the LCMS:

$$C(\mathbf{q}) = 1 + \lambda \exp(-R_{out}^2 q_{out}^2 - R_{side}^2 q_{side}^2 - R_{long}^2 q_{long}^2) \quad (3.19)$$

666 where  $q_{out}$ ,  $q_{side}$ ,  $q_{long}$  are  $\mathbf{q}$  components in the outward, sideward and longitudinal direction. The  $\lambda$  parameter in the equations above determines correlation  
 667 strength. The lambda parameter has values in the range  $\lambda \in [-0.5, 1]$  and it depends on a pair type. In case of pairs of identical bosons (like  $\pi-\pi$  or  $K-K$ ) the  
 668 lambda parameter  $\lambda \rightarrow 1$ . For identical fermions (e.g.  $p-p$ )  $\lambda \rightarrow -0.5$ . Values of  
 669  $\lambda$  observed experimentally are lower than 1 (for bosons) and greater than -0.5  
 670 (for fermions). There are few explanations to this effect: detector efficiencies, in-  
 671 clusion of misidentified particles in a used sample or inclusion of non-correlated  
 672 pairs (when one or both particles come from e.g. long-lived resonance). The  
 673 analysis carried out in this work uses data from a model, therefore the detector  
 674 efficiency and particle purity is not taken into account [25].  
 675

### 677 3.2.5 Spherical harmonics decomposition of a correlation function

678 Results coming from an analysis using three-dimensional correlation func-  
 679 tion in Cartesian coordinates are quite difficult to visualize. To do that, one usu-  
 680 ally performs a projection into a one dimension in outward, sideward and lon-  
 681 gitudinal directions. One may loose important information about a correlation  
 682 function in this procedure, because it gives only a limited view of the full three-  
 683 dimensional structure. Recently, a more advanced way of presenting corre-  
 684 lation function - a spherical harmonics decomposition, was proposed. The three-  
 685 dimensional correlation function is decomposed into an infinite set of compo-  
 686 nents in a form of one-dimensional histograms  $C_l^m(q)$ . In this form, a correlation  
 687 function is defined as a sum of a series [26]:  
 688

$$C(\mathbf{q}) = \sum_{l,m} C_l^m(q) Y_l^m(\theta, \phi), \quad (3.20)$$

689 where  $Y_l^m(\theta, \phi)$  is a spherical harmonic function. Spherical harmonics are an  
 690 orthogonal set of solutions to the Laplace's equation in spherical coordinates  
 691 Hence, in this approach, a correlation function is defined as a function of  $q$ ,  $\theta$   
 692 and  $\phi$ . To obtain  $C_l^m$  coefficients in the series, one has to calculate the following  
 693 integral:

$$C_l^m(q) = \int_{\Omega} C(q, \theta, \phi) Y_l^m(\theta, \phi) d\Omega, \quad (3.21)$$

693 where  $\Omega$  is a full solid angle.

Spherical harmonics representation has several important advantages. The main advantage of this decomposition is that it requires less statistics than traditional analysis performed in Cartesian coordinates. Another one is that it encodes full three-dimensional information in a set of one-dimensional plots. In principle it does not have to be an advantage, because full description of a correlation function requires infinite number of  $l, m$  components. But it so happens that the intrinsic symmetries of a pair distribution in a femtoscopic analysis result in most of the components to vanish. For the identical particles correlation functions, all coefficients with odd values of  $l$  and  $m$  disappear. It has also been shown, that the most significant portion of femtoscopic data is stored in the components with the lowest  $l$  values. It is expected that, the main femtoscopic information is contained in the following components [25]:

$$C_0^0 \rightarrow R_{LCMS}, \quad (3.22)$$

$$\Re C_2^0 \rightarrow \frac{R_T}{R_{long}}, \quad (3.23)$$

$$\Re C_2^2 \rightarrow \frac{R_{out}}{R_{side}}, \quad (3.24)$$

694 where  $R_{LCMS} = \sqrt{(R_{out}^2 + R_{side}^2 + R_{long}^2)/3}$  and  $R_T = \sqrt{(R_{out}^2 + R_{side}^2)/2}$ .  
 695 The  $C_0^0$  is sensitive to the overall size of a correlation function. The  $\Re C_2^0$  carries  
 696 the information about the ratio of the transverse to the longitudinal radii, due  
 697 to its  $\cos^2(\theta)$  weighting in  $Y_2^0$ . The component  $\Re C_2^2$  with its  $\cos^2(\phi)$  weighting  
 698 encodes the ratio between outward and sideward radii. Thus, the spherical har-  
 699 monics method allows to obtain and analyze full three-dimensional femtoscopic  
 700 information from a correlation function [25].

### 701 3.3 Experimental approach

702 The correlation function is defined as a probability to observe two particles  
 703 together divided by the product of probabilities to observe each of them sepa-  
 704 rately (Eq. 3.16). Experimentally this is achieved by dividing two distributions  
 705 of relative momentum of pairs of particles coming from the same event and the  
 706 equivalent distribution of pairs where each particle is taken from different colli-  
 707 sions. In this way, one obtains not only femtoscopic information but also all other  
 708 event-wide correlations. This method is useful for experimentalists to estimate  
 709 the magnitude of non-femtoscopic effects. There exists also a different approach,  
 710 where two particles in pairs in the second distribution are also taken from the  
 711 same event. The second method gives only information about physical effects  
 712 accessible via femtoscopy. The aim of this work is a study of effects coming from  
 713 two particle interferometry, hence the latter method was used.

714 In order to calculate experimental correlation function, one uses the follow-  
 715 ing approach. One has to construct two histograms: the *numerator*  $N$  and the

716 denominator  $D$  with the particle pairs momenta, where particles are coming from  
 717 the same event. Those histograms can be one-dimensional (as a function of  $|\mathbf{q}|$ ),  
 718 three dimensional (a function of three components of  $\mathbf{q}$  in LCMS) or a set of one-  
 719 dimensional histogram representing components of the spherical harmonic de-  
 720 composition of the distribution. The second histogram,  $D$  is filled for each pair  
 721 with the weight 1.0 at a corresponding relative momentum  $\mathbf{q} = 2\mathbf{k}^*$ . The first one,  
 722  $N$  is filled with the same procedure, but the weight is calculated as  $|\Psi_{ab}(\mathbf{r}^*, \mathbf{k}^*)|^2$ .  
 723 A division  $N/D$  gives the correlation function  $C$ . This procedure can be simply  
 724 written as [25]:

$$C(\mathbf{k}^*) = \frac{N}{D} = \frac{\sum_{n_i \in D} \delta(\mathbf{k}^* i - \mathbf{k}^*) |\Psi_{ab}(\mathbf{r}^* i, \mathbf{k}^* i)|^2}{\sum_{n_i \in D} \delta(\mathbf{k}^* i - \mathbf{k}^*)} . \quad (3.25)$$

The  $D$  histogram represents the set of all particle pairs used in calculations.  
 The  $n_i$  is a pair with the its relative momentum  $\mathbf{k}^* i$  and relative separation  $\mathbf{r}^* i$ .  
 The wave function used in Eq. 3.25 has one of the following forms:

$$|\Psi_{\pi\pi}(\mathbf{r}^*, \mathbf{k}^*)|^2 = |\Psi_{KK}(\mathbf{r}^*, \mathbf{k}^*)|^2 = 1 + \cos(2\mathbf{k}^* \mathbf{r}^*) , \quad (3.26)$$

$$|\Psi_{pp}(\mathbf{r}^*, \mathbf{k}^*)|^2 = 1 - \frac{1}{2} \cos(2\mathbf{k}^* \mathbf{r}^*) . \quad (3.27)$$

725 The first one is used in case of bosons, and the latter one is for identical fermi-  
 726 ons. Mathematically, the procedure of calculating the Eq. 3.25 is equivalent to a  
 727 calculation of an integral in Eq. 3.17 through a Monte-Carlo method.

### 728 3.4 Scaling of femtoscopic radii

729 In the hydrodynamic models describing expansion of a quark-gluon plasma,  
 730 particles are emitted from the source elements. Each of the source elements is  
 731 moving with the velocity  $u_\mu$  given by hydrodynamic equations. Because solu-  
 732 tions of those equations are smooth, nearby source elements have similar velo-  
 733 cities. Each emitted particle from a certain source element is boosted with the  
 734 flow velocity  $u_\mu$  according to the point of origin. Hence particles emitted close  
 735 to each other (pairs with large transverse momentum  $|\mathbf{k}_T|$ ) will gain the similar  
 736 velocity boost, they can combine into pairs with small relative momenta ( $|\mathbf{q}|$ ) and  
 737 therefore become correlated. If the two particles are emitted far away from each  
 738 other (a pair with small  $|\mathbf{k}_T|$ ), the flow field  $u_\mu$  in their point of emission might  
 739 be very different and it will be impossible for them to have sufficiently small rel-  
 740 ative momenta in order to be in region of interference effect. This effect is visible  
 741 in a width of a correlation function in the Fig. 3.4. The correlation function gets  
 742 broader for greater values of  $|\mathbf{k}_T|$  and the femtoscopic radius  $R$  becomes smal-  
 743 ler [8, 27].

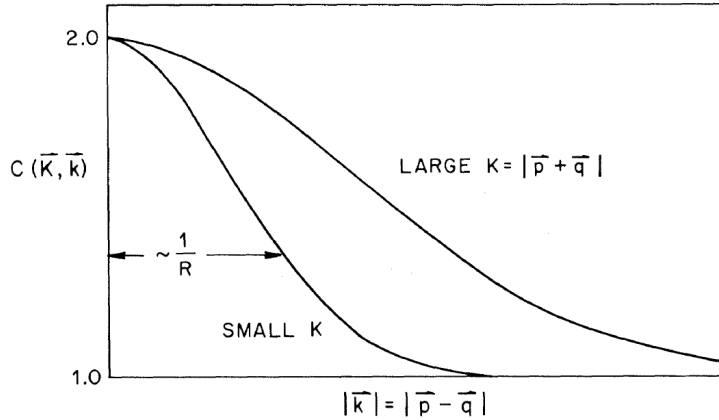


Figure 3.4: Correlation function width dependence on total pair momentum. Pion pairs with a large total momentum are more correlated [27].

#### 744 3.4.1 Scaling in LCMS

Hydrodynamic calculations performed in LCMS show that femtoscopic radii in outward, sideward, and longitudinal direction show dependence on transverse mass  $m_T = \sqrt{k_T^2 + m^2}$ , where  $m$  is a mass of a particle [28]. Moreover, experimental results show that this scaling is observed for  $R_{LCMS}$  radii also. This dependence can be expressed as follows:

$$R_i = \alpha m_T^{-\beta} \quad (3.28)$$

745 where  $i$  subscript indicates that this equation applies to  $R_{out}$ ,  $R_{side}$  and  $R_{long}$   
 746 radii. The  $\beta$  exponent is approximately equal 0.5. In case of strong transversal  
 747 expansion of the emitting source, the decrease of longitudinal interferometry ra-  
 748 dius can be more quick than  $m_T^{-0.5}$ , hence one can expect for longitudinal radii  
 749 greater values of  $\beta > 0.5$  [28].

#### 750 3.4.2 Scaling in PRF

751 In the collisions at the LHC energies, pions are most abundant particles and  
 752 their multiplicities are large enough to enable three-dimensional analysis. How-  
 753 ever, for heavier particles, such as kaons and protons statistical limitations arise.  
 754 Hence it is often possible to only measure one-dimensional radius  $R_{inv}$  for those  
 755 particles. The  $R_{inv}$  is then calculated in the PRF. The transition from LCMS to  
 756 PRF is a Lorentz boost in the direction of pair transverse momentum with velo-  
 757 city  $\beta_T = p_T/m_T$ . Hence only  $R_{out}$  radius changes:

$$R_{out}^* = \gamma_T R_{out}. \quad (3.29)$$

758 The one-dimensional  $R_{inv}$  radius is direction-averaged source size in PRF. One  
 759 can notice, that such power-law scaling of  $R_{inv}$  described by Eq. 3.28 is not

760 observed. To recover such scaling in PRF one has to take into consideration two  
 761 effects when transforming variables from LCMS to PRF: overall radius growths  
 762 and source distribution becomes non-Gaussian, while developing long-range  
 763 tails (see Fig. 3.3 for an example). The interplay of these two effects can be  
 764 accounted with an approximate formula:

$$R_{inv} = \sqrt{(R_{out}^2 \sqrt{\gamma_T} + R_{side}^2 + R_{long}^2)/3} . \quad (3.30)$$

Assuming that all radii are equal  $R_{out} = R_{side} = R_{long}$  this formula can be simplified:

$$R_{LCMS} \approx R_{inv} \times [(\sqrt{\gamma_T} + 2)/3]^{-1/2} . \quad (3.31)$$

765 This approximate formula allows to restore power-law behaviour of the scaled  
 766 radii not only when the radii are equal, but also when their differences are small  
 767 (for explanation see the last part of the section 3.2.3).

768 This method of recovering scaling in PRF can be used as a tool for the search  
 769 of hydrodynamic collectivity between pions, kaons and protons in heavy ion col-  
 770 lisions with the measurement of one-dimensional radius in PRF.

771 **Chapter 4**

772 **Results**

773 For the purposes of the femtoscopic analysis in this thesis, the THERMINATOR  
774 model was used to generate large number of events for eight different sets of  
775 initial conditions corresponding the following centrality ranges: 0-5%, 0-10%, 10-  
776 20%, 20-30%, 30-40%, 40-50%, 50-60% and 60-70% for the Pb-Pb collisions at the  
777 centre of mass energy  $\sqrt{s_{NN}} = 2.76 \text{ TeV}$ .

778 **4.1 Identical particles correlations**

779 The correlation functions (three-dimensional and one-dimensional) were cal-  
780 culated separately for the following different pairs of identical particles:  $\pi-\pi$ ,  $K-$   
781  $K$  and  $p-p$  for nine  $k_T$  bins (in GeV/c): 0.1-0.2, 0.2-0.3, 0.3-0.4, 0.4-0.5, 0.6-0.7,  
782 0.7-0.8, 0.8-1.0 and 1.0-1.2. In case of kaons,  $k_T$  ranges start from 0.3 and for pi-  
783 ons from 0.4 and for both of them the maximum value is 1.0. The  $k_T$  ranges for  
784 the heavier particles were limited to maintain sufficient multiplicity to perform  
785 reliable calculations.

786 **4.1.1 Spherical harmonics components**

787 The three-dimensional correlation function as a function of relative  
788 momentum  $q_{LCMS}$  was calculated in a form of components of spherical  
789 harmonics series accordingly to the Eq. 3.21. In the femtoscopic analysis of  
790 identical particles, the most important information is stored in the  $\Re C_0^0$ ,  $\Re C_2^0$   
791 and  $\Re C_2^2$ , hence only those components were analyzed. Correlation functions  
792 obtained in this procedure were calculated for the different centrality bins for the  
793 pairs of pions, kaons and protons. They are presented in the Fig. 4.1, 4.2 and 4.3.

794 Coefficients for pairs of identical bosons (pions and kaons) are shown in the  
795 Fig. 4.1 and 4.2. The wave function symmetrization (Bose-Einstein statistics)  
796 causes the increase of a correlation in the low relative momenta regime ( $q_{LCMS} <$   
797 0.06 GeV/c or even  $q_{LCMS} < 0.12 \text{ GeV/c}$  for more peripheral collisions). It is  
798 clearly visible in the  $\Re C_0^0$  component. The  $\Re C_0^0$  resembles one-dimensional cor-

relation function and in fact it encodes information about overall source radius. The second coefficient  $\Re C_2^0$  differs from zero (is negative), which yields the information about the ratio  $R_T/R_{long}$ . The  $\Re C_2^2$  stores the  $R_{out}/R_{side}$  ratio and one can notice that is non-vanishing (is also negative).

The correlation function for a pair of identical fermions is presented in the Fig. 4.3. An influence of wave function anti-symmetrization (Fermi-Dirac statistics) has its effect in the decrease of a correlation down to 0.5 at low relative momentum ( $q_{LCMS} < 0.1 \text{ GeV/c}$  or  $q_{LCMS} < 0.15 \text{ GeV/c}$  for more peripheral collisions), which can be observed in  $\Re C_0^0$ . The  $\Re C_2^0$  and  $\Re C_2^2$  coefficients differ from zero and are becoming positive.

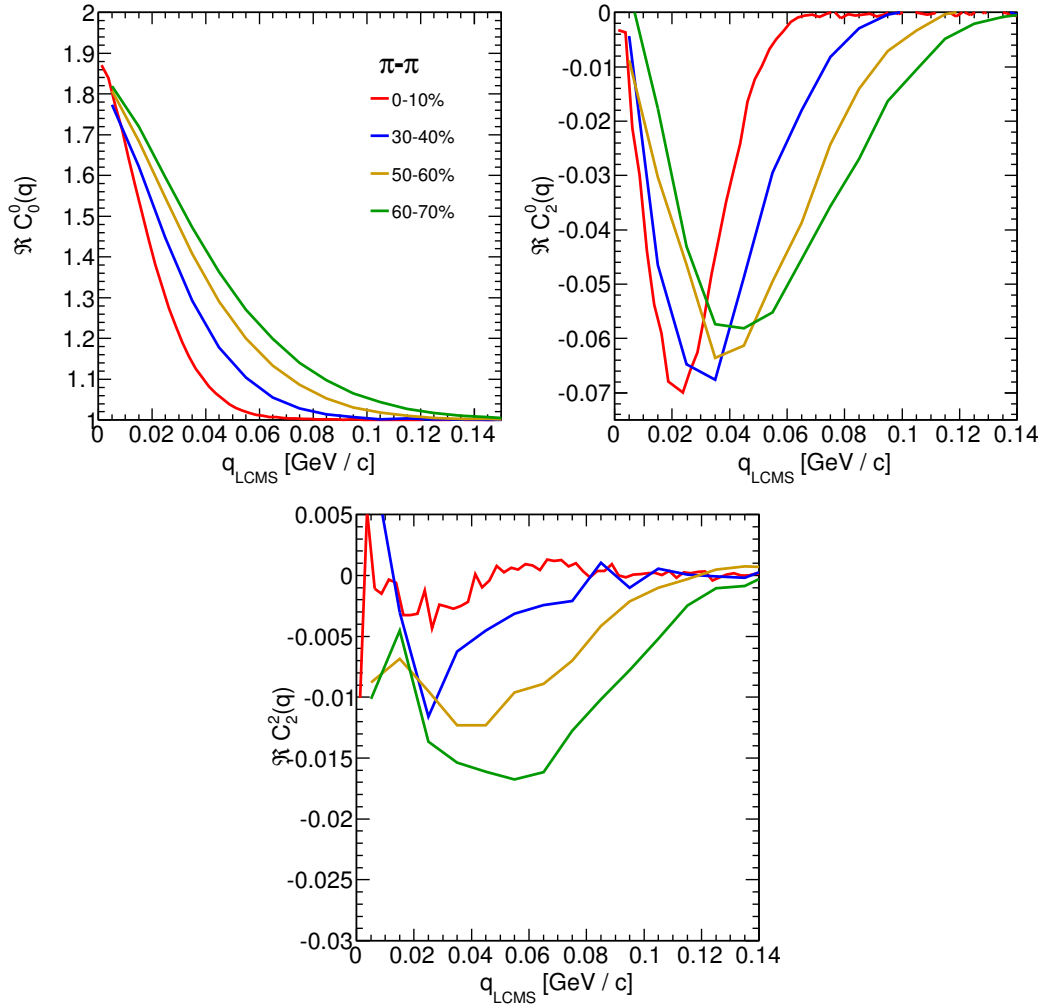


Figure 4.1: Spherical harmonics coefficients of the two-pion correlation function. From the top left:  $\Re C_0^0$ ,  $\Re C_2^0$  and  $\Re C_2^2$ . Only few centrality bins are presented for increased readability.

809     The common effect of the spherical harmonics form of a correlation function  
 810    is the “mirroring” of the shape of the  $\Re C_0^0$  coefficient - when correlation func-  
 811    tion increases at low  $q_{LCMS}$ , the  $\Re C_2^0$  and  $\Re C_2^2$  are becoming negative and vice  
 812    versa. This is quite different behaviour than in the case of correlations of non-  
 813    identical particles, where the  $\Re C_2^0$  still behaves in the same manner, but  $\Re C_2^2$  has  
 814    the opposite sign to the  $\Re C_2^0$  [25].

815     In all cases, the correlation function gets wider with the peripherality of a  
 816    collision i.e. the correlation function for most central collisions (0-10%) is much  
 817    narrower than for the most peripheral ones (60-70%). This phenomena in clearly

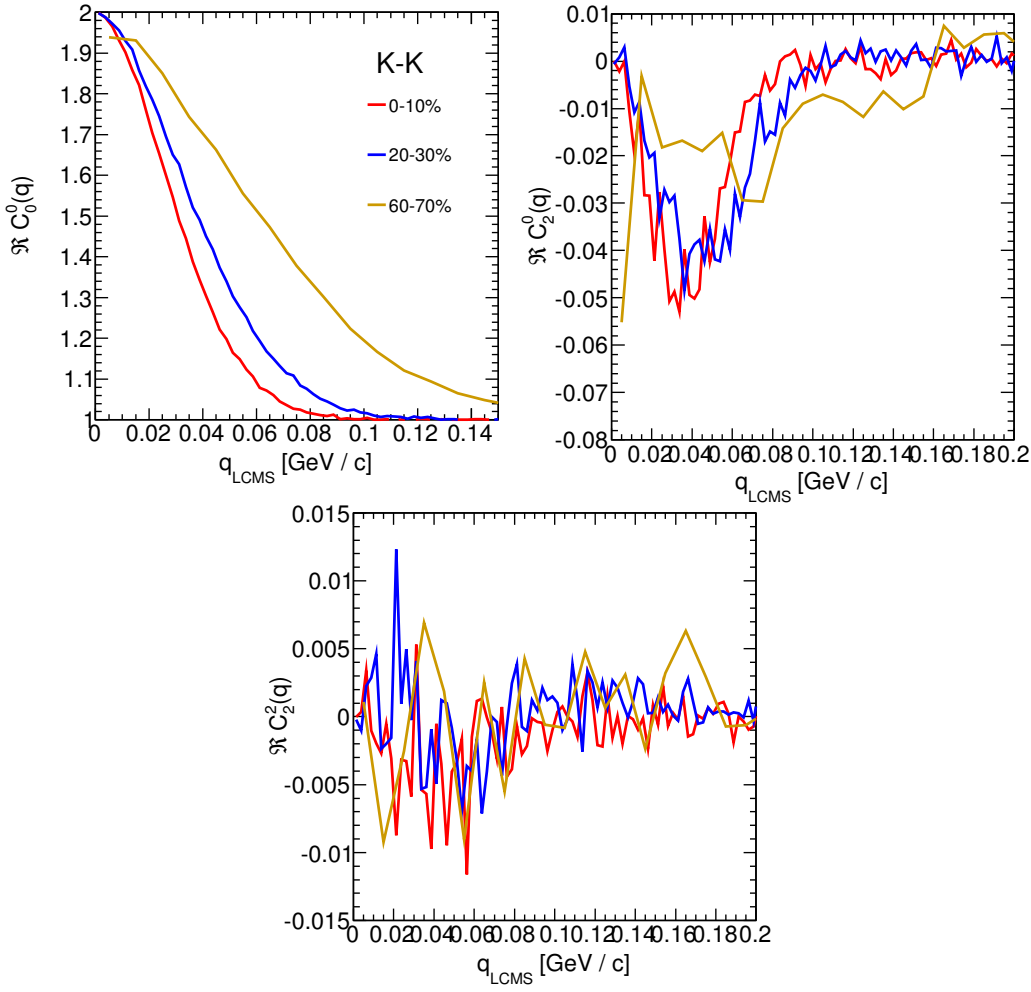


Figure 4.2: Spherical harmonics coefficients of the two-kaon correlation function. From the top left:  $\Re C_0^0$ ,  $\Re C_2^0$  and  $\Re C_2^2$ . Only few centrality bins are presented for increased readability. The  $\Re C_2^2$  is noisy, but one can still notice that it differs from zero and is becoming negative.

visible the  $\Re C_0^0$  coefficients. Other components are also affected by this effect, this is especially noticeable in the case of kaons and pions. For the protons, the results are noisy, hence this effect is not clearly distinguishable.

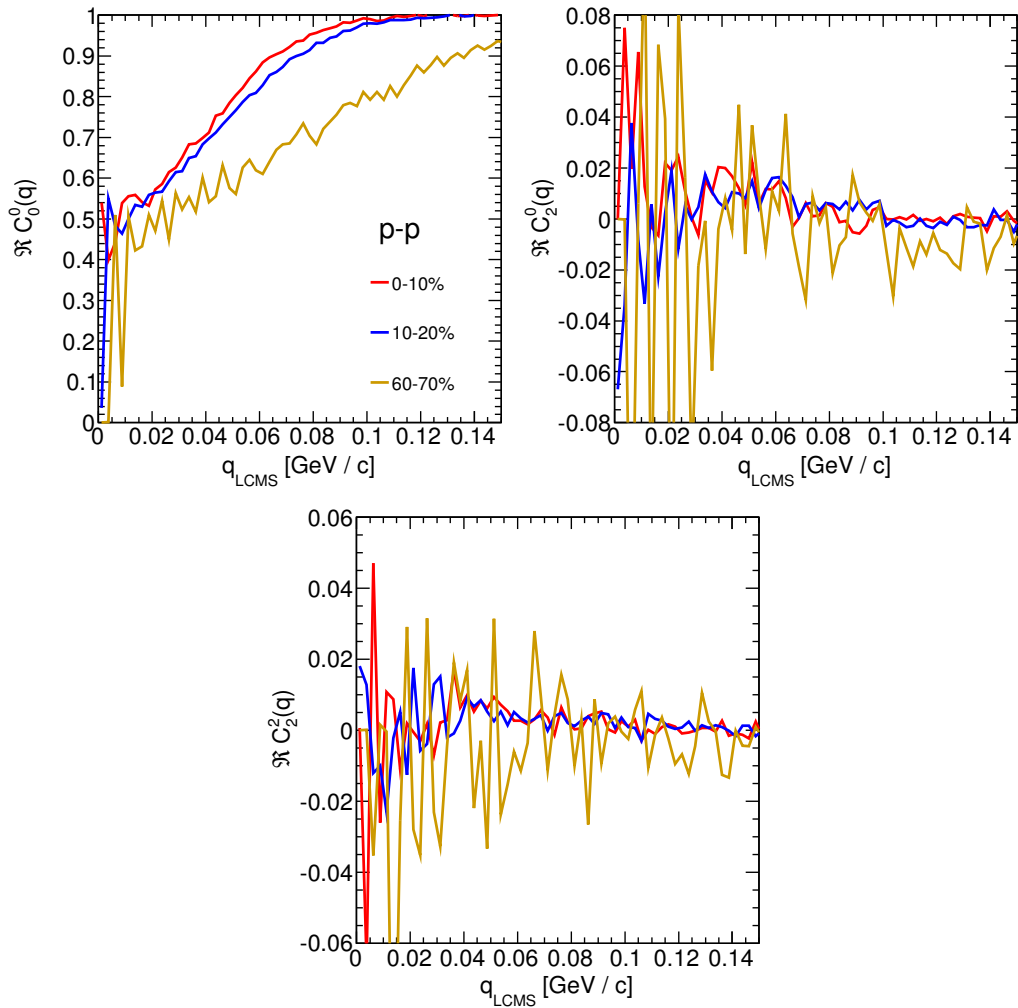


Figure 4.3: Spherical harmonics coefficients of the two-proton correlation function. From the top left:  $\Re C_0^0$ ,  $\Re C_2^0$  and  $\Re C_2^2$ . Only few centrality bins are presented for increased readability. The  $\Re C_2^0$  and  $\Re C_2^2$  are noisy, but one can still notice, that they differ from zero and are becoming positive.

821 **4.1.2 Centrality dependence of a correlation function**

822 The centrality dependence of a correlation function is especially visible in  
 823 one-dimensional correlation functions. This effect is presented in the Fig. 4.4 -  
 824 the correlation functions for pions, kaons and protons are plotted for the same  
 825  $k_T$  range but different centrality bins. One can notice that the width of a func-  
 826 tion is smaller in the case of most central collisions. Hence, the femtoscopic radii  
 827 (proportional to the inverse of width) are increasing with the centrality. An ex-  
 828 planation for this growth is that in the most central collisions, a size of a created  
 system is larger than for the peripheral ones.

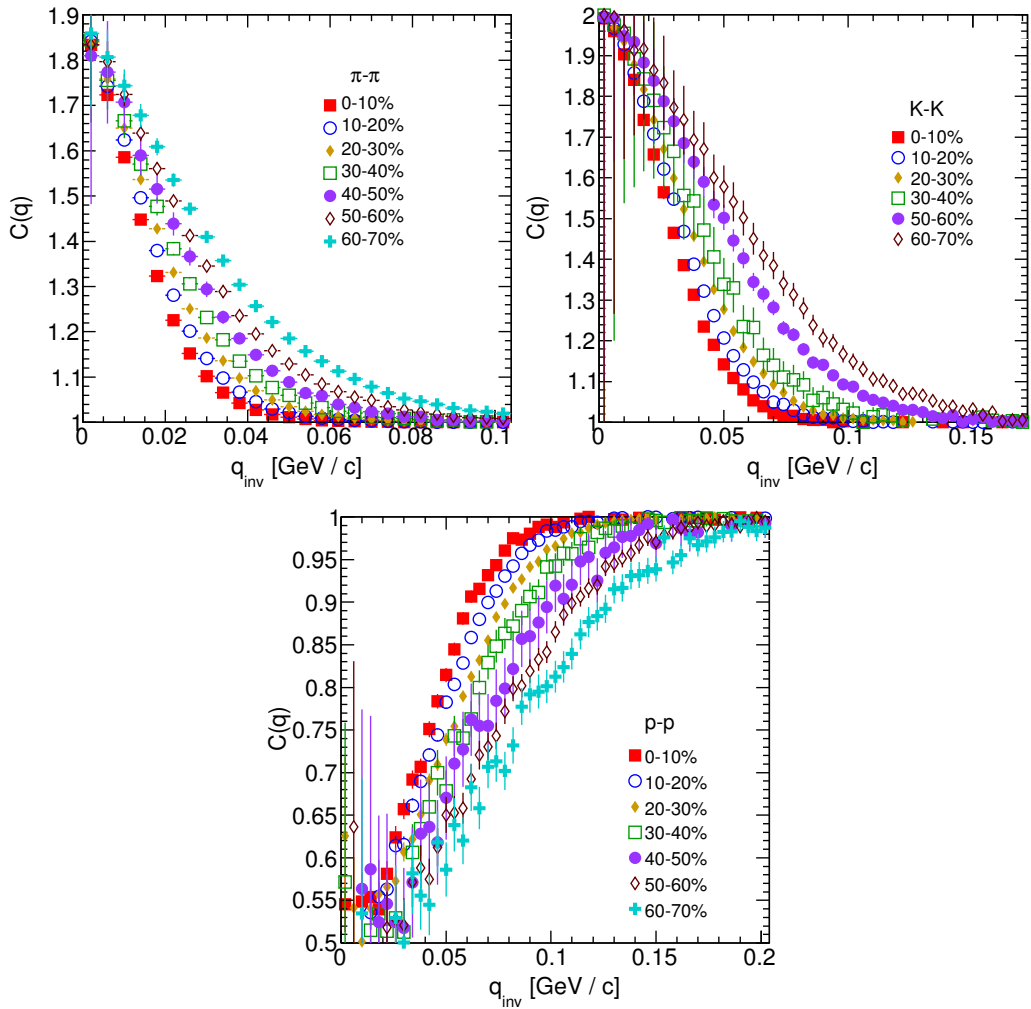


Figure 4.4: One-dimensional correlation function for pions (top left), kaons (top right) and protons (bottom) for different centralities.

### 4.1.3 $k_T$ dependence of a correlation function

In the Fig. 4.5 there are presented one-dimensional correlation functions for pions, kaons and protons for the same centrality bin, but different  $k_T$  ranges. One can observe in all cases of the particle types, appearance of the same trend: with the increase of the total transverse momentum of a pair, the width of a correlation function increases and the femtoscopic radius decreases. The plots in the Fig. 4.5 were zoomed in to show the influence of  $k_T$ .

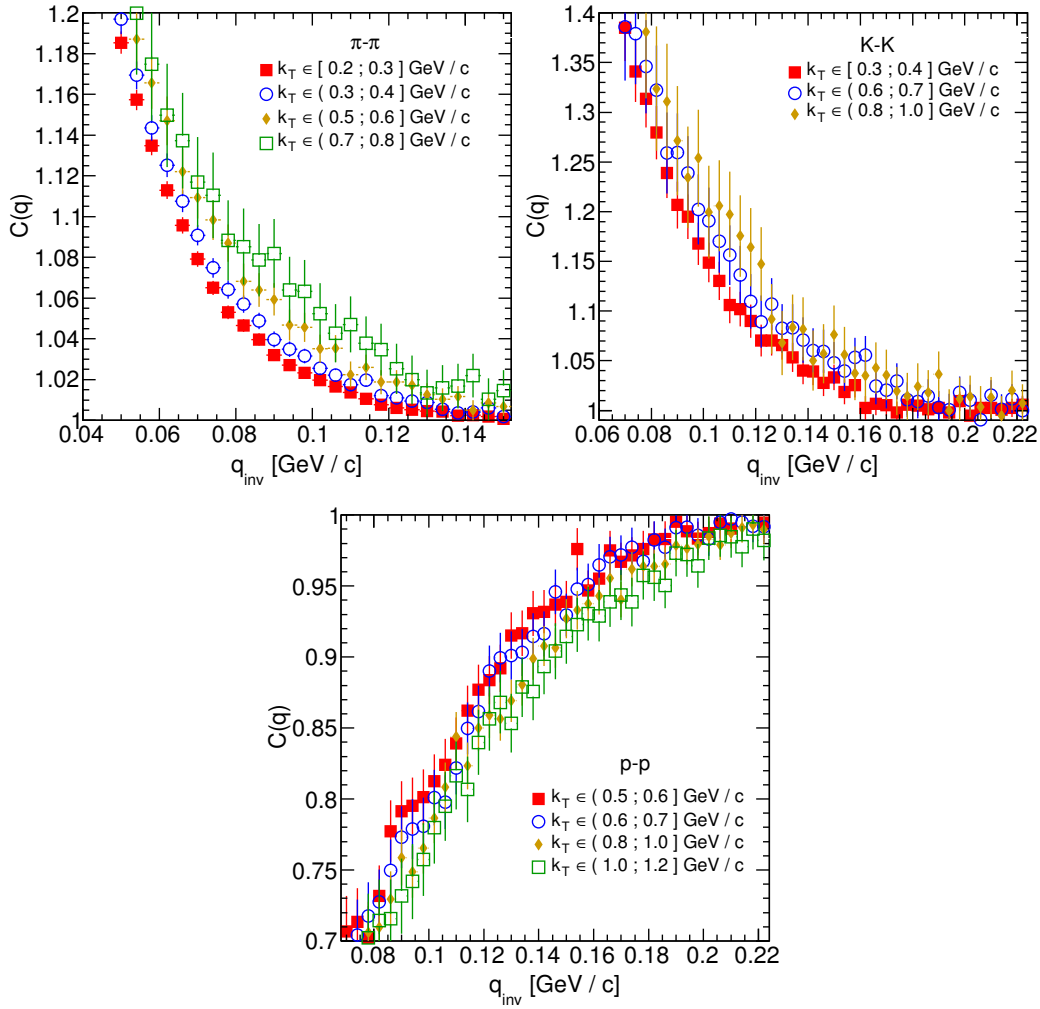


Figure 4.5: One-dimensional correlation functions for pions, kaons and protons, for the same centrality bin and different  $k_T$  ranges. The plot was zoomed in to the region which illustrates the  $k_T$  dependence in the best way. Only few of the calculated ranges are presented for better readability.

## 4.2 Results of the fitting procedure

In order to perform a quantitative analysis of a wide range of correlation functions, the theoretical formulas were fitted to the calculated experimental-like data. In this procedure, the femtoscopic radii for the three-dimensional as well as one-dimensional correlation functions were extracted. The main goal of this analysis is a verification of a common transverse mass scaling for different particles types. Obtained radii are plotted as a function of a transverse mass  $m_T = \sqrt{k_T^2 + m^2}$ . To test the scaling, the following power-law was fitted to the particular radii afterwards:

$$R_x = \alpha m_T^{-\beta}, \quad (4.1)$$

where the  $\alpha$  and  $\beta$  are free parameters.

### 4.2.1 The three-dimensional femtoscopic radii scaling

In the Fig. 4.6 there are presented femtoscopic radii in the outward, sideward and longitudinal directions for the analysis of two-pion correlation functions in

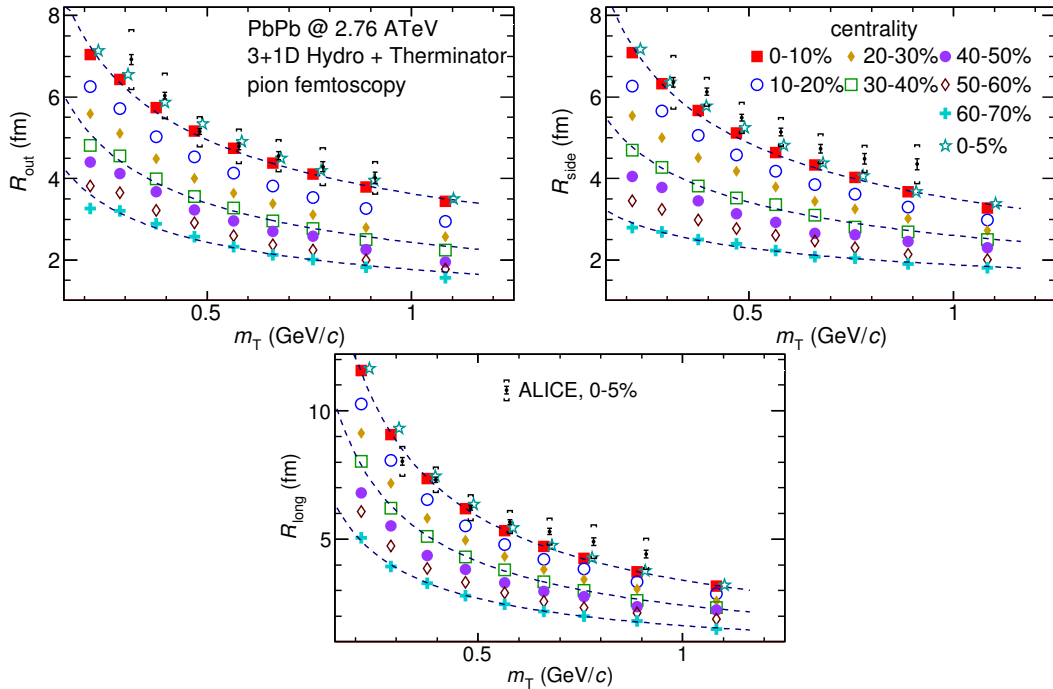


Figure 4.6: Femtoscopic radii in LCMS coming from two-pion correlation functions for all centrality bins as a function of  $m_T$ . The dashed lines are power-law fits. The most central collisions (0-5%) are compared to the results from ALICE [29]. The two datasets are shifted to the right for visibility [30].

the LCMS. The dashed lines are fits of the power law to the data. One can notice, that the power law describes well data points with a 5% accuracy. The  $\beta$  fit parameter for the outward direction is in the order of 0.45. For the sideward direction, this parameter has the similar value, but it is lower for the most peripheral collisions. In case of the longitudinal direction, the  $\beta$  has greater value, up to 0.75. In the Fig. 4.6 there are also compared results for the top 5% central collisions (star-shaped markers) with experimental data from ALICE [29]. The experimental results are consistent with the ones coming from the model predictions.

The Fig. 4.7 presents femtoscopic radii coming from the kaon calculations. The  $R_{out}$ ,  $R_{side}$  and  $R_{long}$  fall also with the power-law within the 5% accuracy. The  $\beta$  parameter was larger in case of kaons: 0.59 in outward direction, 0.54 in the sideward and 0.86 for longitudinal.

The results for two-proton analysis are shown in the Fig. 4.8. The Eq. 4.1 was fitted to the data and tells that the protons also follow the  $m_T$  scaling within 5% range. The  $\beta$  parameter values were even bigger for the outward ( 0.58 ), sideward ( 0.61 ) and longitudinal ( 1.09 ) directions than for the other particle types.

The Fig. 4.9 presents results for the pions, kaons and protons together as a function of  $m_T$ . Considering differences in the  $\beta$  value for the fits for differ-

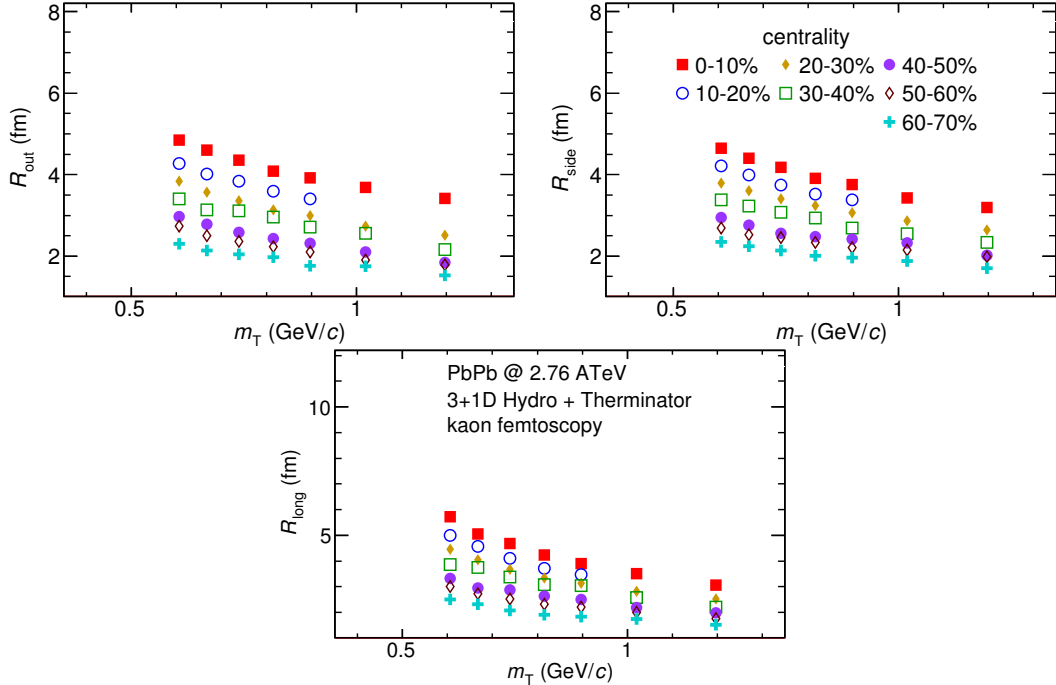


Figure 4.7: Femtoscopic radii extracted from two-kaon correlation functions for different centrality bins as a function of  $m_T$ . [30].

ent particles, one can suspect that there is no common scaling between different kinds of particles. However, when all of the results shown on the same plot, they are aligning on the common curve and the scaling is well preserved. The scaling accuracy is 3%, 5% and 4% for the 0-10%, 20-30% and 60-70% for the outward direction. For the sideward radii the scaling is better, with average deviations 2%, 2% and 3% respectively. In case of longitudinal direction the accuracy is 6%, 5% and 3% for the three centralities. The  $\beta$  parameter for the outward direction is close to the 0.42 in all cases. For the sideward direction it varies from 0.28 to 0.47 and is bigger for more central collisions. Regarding longitudinal radii, the exponent is bigger than the other two:  $\beta \in [0.62; 0.72]$ . Considering all results, the plotted radii are following the common power-law scaling within the 5% accuracy for all directions, centralities and particle types.

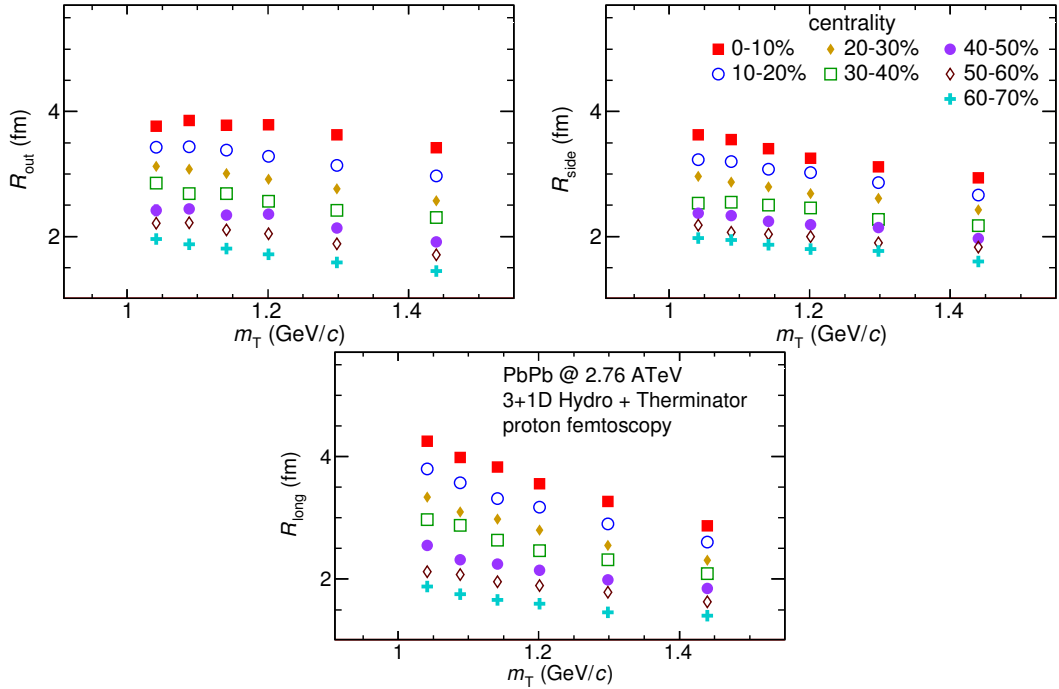


Figure 4.8: Femtoscopic radii extracted from two-proton correlation functions for different centrality bins as a function of  $m_T$ . [30].

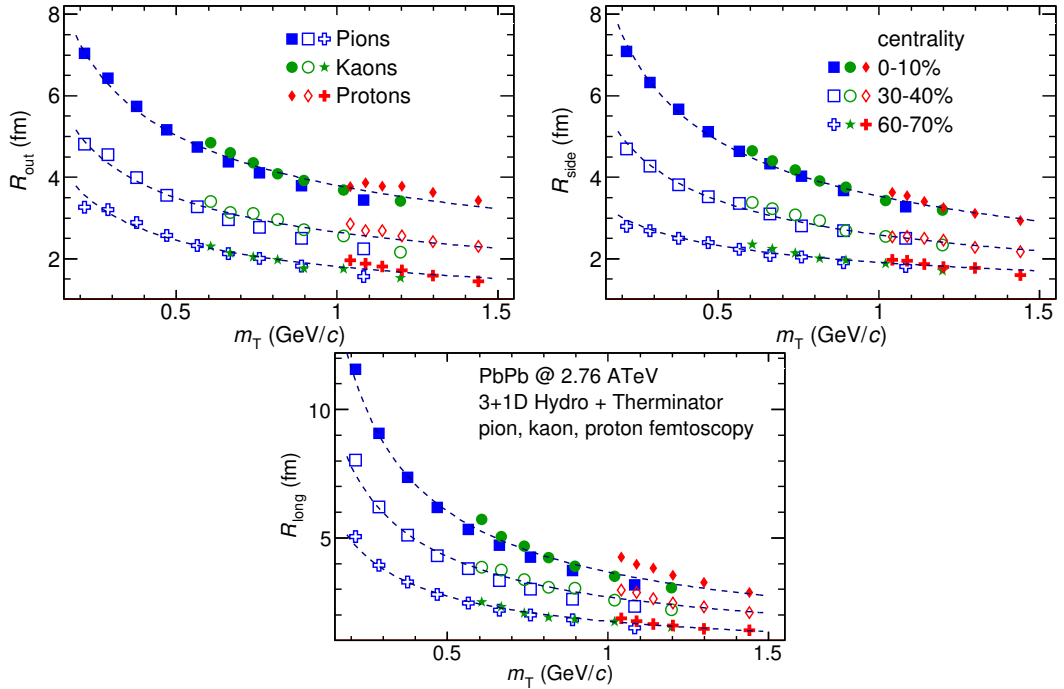


Figure 4.9: The results from the calculations for the pions, kaons and protons in for the three centralities presented on the common plot. One can notice that radii for particular centralities and different particle types follow the common power-law scaling. [30].

### 4.2.2 Scaling of one-dimensional radii

To the one-dimensional correlation function, the corresponding function in the PRF given by the Eq. 3.18 was fitted. The results from those fits are presented in the upper left plot in the Fig. 4.10. One immediately notices, that there is no common scaling of  $R_{inv}$  for different kind of particles. In the Fig. 4.9 the radii in the outward direction for the pions, kaons and protons for the same  $m_T$  are similar. However, when one performs a transition from the LCMS to the PRF, the  $R_{out}$  radius grows:

$$R_{out}^* = \gamma_T R_{out}, \quad (4.2)$$

where  $\gamma_T = m_T/m$ . For the lighter particles, the  $\gamma_T$  is much larger, hence the bigger growth of the  $R_{out}$  and the overall radius. This is visible in the Fig. 4.10 (top left), where the radii in the PRF for the lighter particles are bigger than for the heavier ones in case of the same  $m_T$  range.

In the Fig. 4.9 there is visible scaling in the outward, sideward and longitudinal direction. Hence one can expect an appearance of such scaling in a direction-averaged radius calculated in the LCMS. This radius is presented in the Fig. 4.10 (bottom) and indeed the  $R_{LCMS}$  exhibits power-law scaling with the  $m_T$ .

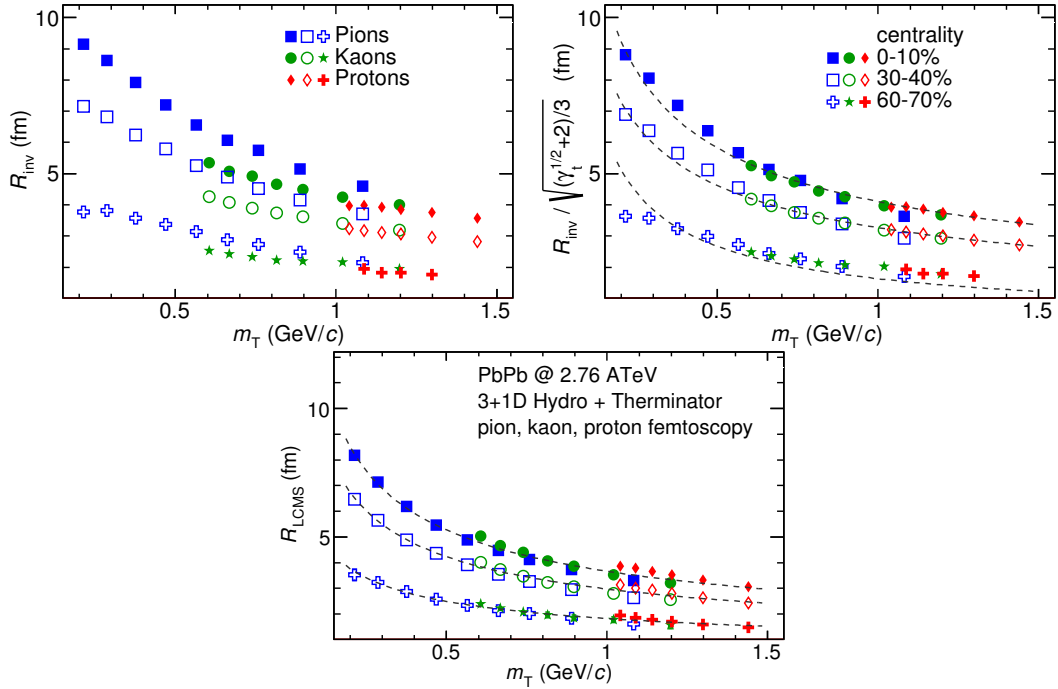


Figure 4.10: Top left: one-dimensional radius for pions, kaons and protons calculated in the PRF. Top right: the  $R_{inv}$  scaled by the proposed factor. Bottom: averaged one-dimensional radius in the LCMS for pions, kaons and protons. Only three centrality bins are shown for the better readability [30].

898 One can try to account the effect of an increase of the radii in the outward  
 899 direction by using the appropriate scaling factor. In the Fig. 4.10 (top right) there  
 900 are femtoscopic radii in the LCMS divided by the proposed scaling factor:

$$f = \sqrt{(\sqrt{\gamma_T} + 2)/3} . \quad (4.3)$$

901 The radii for pions, kaons and protons in the PRF after the division by  $f$  are  
 902 following the power-law with the accuracy of 10%.

### 903 4.3 Discussion of the results

904 The femtoscopic radii obtained from the three-dimensional correlation func-  
 905 tion fitting exhibit the  $m_T$  dependence described by the power law (Eq. 4.1). This  
 906 scaling is preserved quite well with accuracy <10%. Observation of such scaling  
 907 in a femtoscopic radii is a strong signal of appearance of a collective behaviour of  
 908 a particle-emitting source created in the collision. The data used in the analysis  
 909 was coming from the hydrodynamic model, hence one can indeed expect the  
 910 appearance of this scaling. However, the results for pion femtoscopy from the  
 911 ALICE at LHC are consistent with the data from analysis performed in this thesis  
 912 (Fig. 4.6). This is a confirmation of an applicability of hydrodynamic models in a  
 913 description of an evolution of a quark-gluon plasma.

914 The  $\beta$  parameter calculated in the fitting of the power-law to the femtoscopic  
 915 radii is in the order of 0.5 in case of the radii in the transverse plane. This value is  
 916 consistent with the hydrodynamic predictions. In case of longitudinal radii, the  
 917 exponent is bigger (greater than 0.7), which is an indication of a strong transversal  
 918 expansion in the system [28].

919 A scaling described above is visible in the LCMS, however due to limited stat-  
 920 istics, analysis in this reference frame is not always possible. In such case one per-  
 921 forms calculations in the PRF. The  $m_T$  scaling in the PRF is not observed - this has  
 922 the trivial kinematic origin. A transition from the PRF to LCMS causes growth  
 923 of the radius in the outward direction and the common power-law scaling for  
 924 different particles breaks due to differences in the  $\gamma_T(m_T)$  for different particle  
 925 types. However one can try to deal with the radius growth and restore the scal-  
 926 ing by multiplying the radii  $R_{inv}$  by an approximate factor  $\sqrt{(\sqrt{\gamma_T} + 2)/3}$ . The  
 927 scaled  $R_{inv}$  are following the power-law and could be used as a verification of  
 928 hydrodynamic behaviour in the investigated particle source.

929 The hadronic evolution and freeze-out in the THERMINATOR is followed  
 930 by the resonance propagation and decay phase. A good accuracy of a scaling  
 931 with the power-law indicated that the inclusion of the resonances does not  
 932 break the  $m_T$  scaling. However, recent calculations including also hadron  
 933 rescattering phase indicate that the scaling between pions and kaons is broken  
 934 at the LHC [31].

# 935 Conclusions

936 This thesis presents the results of the two-particle femtoscopy of different  
937 particle kinds produced in Pb-Pb collisions at the centre of mass energy  
938  $\sqrt{s_{NN}} = 2.76$  TeV. The analysed data was generated by the THERMINATOR  
939 model using the (3+1)-dimensional hydrodynamic model.

940 The momentum correlations were studied for three different types of particle  
941 pairs: pions, kaons and protons. The data was analyzed for eight different sets  
942 of initial conditions corresponding the following centrality ranges: 0-5%, 0-10%,  
943 10-20%, 20-30%, 30-40%, 40-50%, 50-60% and 60-70%. The correlation functions  
944 were calculated for the nine  $k_T$  bins from 0.1 GeV/c to 1.2 GeV/c. The cal-  
945 culations were performed using spherical harmonics decomposition of a three-  
946 dimensional correlation function. Using this approach, one can obtain full three-  
947 dimensional information about the source size using only the three coefficients:  
948  $\Re C_0^0$ ,  $\Re C_2^0$  and  $\Re C_2^2$ . To perform further quantitative analysis, the femtoscopic  
949 radii were extracted through fitting.

950 The calculated correlation functions show expected increase of a correlation  
951 at low relative momenta in case of identical bosons (pions and kaons) and the  
952 decrease for the identical fermions (protons) respectively. This effect is especially  
953 visible in the first spherical harmonic coefficient  $\Re C_0^0$ . The other two components  
954  $\Re C_2^0$  and  $\Re C_2^2$  are non-vanishing and are providing information about the ratios  
955 of radii in the outward, sideward and longitudinal directions.

956 An increase of width of a correlation function with the peripherality of a colli-  
957 sion and the  $k_T$  is observed for pions, kaons and protons. This increase of femto-  
958scopic radii (proportional to the inverse of width) with the  $k_T$  is related with the  
959  $m_T$  scaling predicted by the hydrodynamic calculations.

960 Hydrodynamic equations are predicting appearance of femtoscopic radii  
961 common scaling for different kinds of particles with the  $m_T^{-0.5}$  in the LCMS.  
962 In the results in this work, a common scaling for different particle types is  
963 observed in the LCMS in the outward, sideward and longitudinal direction. The  
964 direction-averaged radius  $R_{LCMS}$  also shows this power-law behaviour. The  
965 fitting of a power law  $\alpha m_T^{-\beta}$  to the femtoscopic radii yielded the information,  
966 that the  $\beta$  exponent for the outward and sideward direction is in order of 0.5,  
967 which is consistent with the hydrodynamic predictions. For the longitudinal  
968 direction, the  $\beta$  is bigger ( $>0.7$ ) than in the other directions which is an indication  
969 of a strong transverse flow. Femtoscopic radii in LCMS are following the

970 power-law scaling with the accuracy <5% for pions and kaons, and <10% in case  
971 of protons.

972 In case of the one-dimensional radii  $R_{inv}$  calculated in the PRF, no common  
973 scaling is observed. This is a consequence of a transition from the LCMS to the  
974 PRF, which causes the growth of radius in the outward direction and breaks the  
975 scaling for different particles. However, one can try to correct the influence of  
976 the  $R_{out}$  growth with an approximate factor  $\sqrt{(\sqrt{\gamma_T} + 2)/3}$ . After the division  
977 of the  $R_{inv}$  by the proposed factor, the scaling is restored with an accuracy <10%.  
978 In this way, the experimentally simpler measure of the one-dimensional radii can  
979 be used as a probe for the hydrodynamic collectivity.

980 The THERMINATOR model includes hydrodynamic expansion, statistical had-  
981 ronization, resonance propagation and decay afterwards. The  $m_T$  scaling is pre-  
982 dicted from the pure hydrodynamic calculations. However, this study shows,  
983 that influence of the resonances on this scaling is less than 10%.

# Bibliography

- [1] Standard Model of Elementary Particles - Wikipedia, the free encyclopedia  
[http://en.wikipedia.org/wiki/standard\\_model](http://en.wikipedia.org/wiki/standard_model).
- [2] R. Aaij et al. (LHCb Collaboration). Observation of the resonant character of the  $z(4430)^-$  state. *Phys. Rev. Lett.*, 112:222002, Jun 2014.
- [3] Donald H. Perkins. *Introduction to High Energy Physics*. Cambridge University Press, fourth edition, 2000. Cambridge Books Online.
- [4] G. Odyniec. *Phase Diagram of Quantum Chromo-Dynamics* - course at Faculty of Physics, Warsaw University of Technology, Jun 2012.
- [5] J. Beringer et al. (Particle Data Group). The Review of Particle Physics. *Phys. Rev.*, D86:010001, 2012.
- [6] Z. Fodor and S.D. Katz. The Phase diagram of quantum chromodynamics. 2009.
- [7] F. Karsch. Lattice results on QCD thermodynamics. *Nuclear Physics A*, 698(1-4):199 – 208, 2002.
- [8] Adam Kisiel. *Studies of non-identical meson-meson correlations at low relative velocities in relativistic heavy-ion collisions registered in the STAR experiment*. PhD thesis, Warsaw University of Technology, Aug 2004.
- [9] J. Bartke. *Relativistic Heavy Ion Physics*. World Scientific Pub., 2009.
- [10] W. Florkowski. *Phenomenology of Ultra-Relativistic Heavy-Ion Collisions*. World Scientific, 2010.
- [11] Science Grid This Week, October 25, 2006 - Probing the Perfect Liquid with the STAR Grid  
[http://www.interactions.org/sgtw/2006/1025/star\\_grid\\_more.html](http://www.interactions.org/sgtw/2006/1025/star_grid_more.html).
- [12] K. Grebieszkow. Fizyka zderzeń ciężkich jonów,  
<http://www.if.pw.edu.pl/~kperl/hip/hip.html>.
- [13] Ulrich W. Heinz. From SPS to RHIC: Maurice and the CERN heavy-ion programme. *Phys. Scripta*, 78:028005, 2008.

- 1012 [14] J. Adams et al. Identified particle distributions in pp and Au+Au collisions  
 1013 at  $s(\text{NN})^{**}(1/2) = 200 \text{ GeV}$ . *Phys.Rev.Lett.*, 92:112301, 2004.
- 1014 [15] G. David, R. Rapp, and Z. Xu. Electromagnetic Probes at RHIC-II. *Phys.Rept.*,  
 1015 462:176–217, 2008.
- 1016 [16] A. Marin et al. Dilepton measurements with CERES. *PoS*, CPOD07:034,  
 1017 2007.
- 1018 [17] J. Adams et al. Experimental and theoretical challenges in the search for the  
 1019 quark gluon plasma: The STAR Collaboration’s critical assessment of the  
 1020 evidence from RHIC collisions. *Nucl.Phys.*, A757:102–183, 2005.
- 1021 [18] Adam Kisiel, Tomasz Taluc, Wojciech Broniowski, and Wojciech  
 1022 Florkowski. THERMINATOR: THERMal heavy-IoN generATOR. *Comput.Phys.Commun.*, 174:669–687, 2006.
- 1024 [19] Mikolaj Chojnacki, Adam Kisiel, Wojciech Florkowski, and Wojciech Bro-  
 1025 niowski. THERMINATOR 2: THERMal heavy IoN generATOR 2. *Comput.Phys.Commun.*, 183:746–773, 2012.
- 1027 [20] I. et al (BRAHMS Collaboration) Bearden. Charged meson rapidity distri-  
 1028 butions in central Au + Au collisions at  $\sqrt{s_{NN}} = 200 \text{ GeV}$ . *Phys. Rev. Lett.*,  
 1029 94:162301, Apr 2005.
- 1030 [21] W. Israel and J.M. Stewart. Transient relativistic thermodynamics and kin-  
 1031 etic theory. *Annals of Physics*, 118(2):341 – 372, 1979.
- 1032 [22] Piotr Bożek. Flow and interferometry in (3 + 1)-dimensional viscous hydro-  
 1033 dynamics. *Phys. Rev. C*, 85:034901, Mar 2012.
- 1034 [23] K. Kovtun, P. D. T. Son, and A. O. Starinets. Viscosity in strongly interacting  
 1035 quantum field theories from black hole physics. *Phys. Rev. Lett.*, 94:111601,  
 1036 Mar 2005.
- 1037 [24] Fred Cooper and Graham Frye. Single-particle distribution in the hydro-  
 1038 dynamic and statistical thermodynamic models of multiparticle production.  
 1039 *Phys. Rev. D*, 10:186–189, Jul 1974.
- 1040 [25] Adam Kisiel. Nonidentical-particle femtoscopy at  $\sqrt{s_{NN}} = 200 \text{ GeV}$  in hy-  
 1041 drodynamics with statistical hadronization. *Phys. Rev. C*, 81:064906, Jun  
 1042 2010.
- 1043 [26] Adam Kisiel and David A. Brown. Efficient and robust calculation of femto-  
 1044 scopic correlation functions in spherical harmonics directly from the raw  
 1045 pairs measured in heavy-ion collisions. *Phys.Rev.*, C80:064911, 2009.
- 1046 [27] S. Pratt. Pion Interferometry for Exploding Sources. *Phys.Rev.Lett.*, 53:1219–  
 1047 1221, 1984.

- 1048 [28] S.V. Akkelin and Yu.M. Sinyukov. The HBT-interferometry of expanding  
1049 inhomogeneous sources. *Z.Phys.*, C72:501–507, 1996.
- 1050 [29] K. Aamodt et al. Two-pion Bose-Einstein correlations in central Pb-Pb colli-  
1051 sions at  $\sqrt{s_{NN}} = 2.76$  TeV. *Phys.Lett.*, B696:328–337, 2011.
- 1052 [30] A. Kisiel, M. Galazyn, and P. Bozek. Pion, kaon, and proton femtoscopy in  
1053 Pb–Pb collisions at  $\sqrt{s_{NN}}=2.76$  TeV modeled in 3+1D hydrodynamics. 2014.
- 1054 [31] V.M. Shapoval, P. Braun-Munzinger, Iu.A. Karpenko, and Yu.M. Sinyukov.  
1055 Femtoscopy correlations of kaons in  $Pb + Pb$  collisions at LHC within hy-  
1056 drokinetic model. 2014.

# <sup>1057</sup> List of Figures

1058    1.1	The Standard Model of elementary particles [1]. . . . .	3
1059    1.2	A string break and a creation of a pair quark-anti-quark [4]. . . . .	5
1060    1.3	The coupling parameter $\alpha_s$ dependence on four-momentum transfer $Q^2$ [5]. . . . .	6
1061    1.4	The QCD potential for a pair quark-antiquark as a function of distance for different temperatures. A value of a potential decreases with the temperature [4]. . . . .	6
1064    1.5	A number of degrees of freedom as a function of a temperature [7]. . . . .	7
1065    1.6	Phase diagram coming from the Lattice QCD calculations [8]. . . . .	8
1066    1.7	Left: stages of a heavy ion collision simulated in the UrQMD model. Right: schematic view of a heavy ion collision evolution [8]. . . . .	9
1069    1.8	Overlapping region which is created in heavy ion collisions has an almond shape. Visible x-z plane is a <i>reaction plane</i> . The x-y plane is a <i>transverse plane</i> . The z is a direction of the beam [11]. . . . .	11
1071    1.9	Cross-section of a heavy ion collision in a transverse plane. $\Psi_R$ is an angle between transverse plane and the reaction plane. The $b$ parameter is an <i>impact parameter</i> - a distance between centers of nuclei during a collision. An impact parameter is related with the centrality of a collision and a volume of the quark-gluon plasma [12]. . . . .	12
1077    1.10	<i>Lower:</i> The elliptic flow $v_2$ follows the hydrodynamical predictions for an ideal fluid perfectly. Note that > 99% of all final hadrons have $p_T < 1.5 \text{ GeV}/c$ . <i>Upper left:</i> The $v_2$ plotted versus transverse kinetic energy $KE_T = m_T - m_0 = \sqrt{p_T^2 + m_0^2} - m_0$ . The $v_2$ follows different universal curves for mesons and baryons. <i>Upper right:</i> When scaled by the number of valence quarks, the $v_2$ follows the same universal curve for all hadrons and for all values of scaled transverse kinetic energy [13]. . . . .	13
1085    1.11	Invariant yield of particles versus transverse mass $m_T = \sqrt{p_T^2 + m_0^2}$ for $\pi^\pm$ , $K^\pm$ , $p$ and $\bar{p}$ at mid-rapidity for p+p collisions (bottom) and Au+Au events from 70-80% (second bottom) to 0-5% (top) centrality [14]. . . . .	14

1089	1.12 Thermal photons spectra for the central Au+Au collisions at			
1090	$\sqrt{s_{NN}} = 200$ GeV at computed within different hydrodynamical			
1091	models compared with the pQCD calculations (solid line) and			
1092	experimental data from PHENIX (black dots) [15]. . . . .	15		
1093	1.13 Left: Invariant mass spectrum of $e^+e^-$ pairs in Pb+Au collisions			
1094	at 158A GeV compared to the sum coming from the hadron decays			
1095	predictions. Right: The expectations coming from model calcula-			
1096	tions assuming a dropping of the $\rho$ mass (blue) or a spread of the			
1097	$\rho$ width in the medium (red) [16]. . . . .	16		
1098	1.14 Azimuthal angle difference $\Delta\phi$ distributions for different colliding			
1099	systems at $\sqrt{s_{NN}} = 200$ GeV. Transverse momentum cut: $p_T > 2$			
1100	GeV. For the Au+Au collisions the away-side jet is missing [17]. . .	17		
1101	3.1 Bertsch-Pratt direction naming convention used in heavy ion col-			
1102	lision. . . . .	23		
1103	3.2 The pair wave function is a superposition of all possible states. In			
1104	case of particle interferometry it includes two cases: particles with			
1105	momenta $p_1, p_2$ registered by detectors $A, B$ and $p_1, p_2$ registered			
1106	by $B, A$ respectively. . . . .	24		
1107	3.3 An averaged three-dimensional Gaussian source function with dif-			
1108	ferent widths was averaged into one-dimensional function. To il-			
1109	lustrate deformations, one-dimensional Gaussian distribution was			
1110	fitted. . . . .	27		
1111	3.4 Correlation function width dependence on total pair momentum.			
1112	Pion pairs with a large total momentum are more correlated [27]. .	31		
1113	4.1 Spherical harmonics coefficients of the two-pion correlation func-			
1114	tion. From the top left: $\Re C_0^0$ , $\Re C_2^0$ and $\Re C_2^2$ . Only few centrality			
1115	bins are presented for increased readability. . . . .	34		
1116	4.2 Spherical harmonics coefficients of the two-kaon correlation func-			
1117	tion. From the top left: $\Re C_0^0$ , $\Re C_2^0$ and $\Re C_2^2$ . Only few centrality			
1118	bins are presented for increased readability. The $\Re C_2^2$ is noisy, but			
1119	one can still notice that it differs from zero and is becoming negative. .	35		
1120	4.3 Spherical harmonics coefficients of the two-proton correlation			
1121	function. From the top left: $\Re C_0^0$ , $\Re C_2^0$ and $\Re C_2^2$ . Only few			
1122	centrality bins are presented for increased readability. The $\Re C_2^0$			
1123	and $\Re C_2^2$ are noisy, but one can still notice, that they differ from			
1124	zero and are becoming positive. . . . .	36		
1125	4.4 One-dimensional correlation function for pions (top left), kaons			
1126	(top right) and protons (bottom) for different centralities. . . . .	37		

1127	4.5	One-dimensional correlation functions for pions, kaons and protons, for the same centrality bin and different $k_T$ ranges. The plot was zoomed in to the region which illustrates the $k_T$ dependence in the best way. Only few of the calculated ranges are presented for better readability. . . . .	38
1128	4.6	Femtoscopic radii in LCMS coming from two-pion correlation functions for all centrality bins as a function of $m_T$ . The dashed lines are power-law fits. The most central collisions (0-5%) are compared to the results from ALICE [29]. The two datasets are shifted to the right for visibility [30]. . . . .	39
1129	4.7	Femtoscopic radii extracted from two-kaon correlation functions for different centrality bins as a function of $m_T$ . [30]. . . . .	40
1130	4.8	Femtoscopic radii extracted from two-proton correlation functions for different centrality bins as a function of $m_T$ . [30]. . . . .	41
1131	4.9	The results from the calculations for the pions, kaons and protons in for the three centralities presented on the common plot. One can notice that radii for particular centralities and different particle types follow the common power-law scaling. [30]. . . . .	42
1132	4.10	Top left: one-dimensional radius for pions, kaons and protons calculated in the PRF. Top right: the $R_{inv}$ scaled by the proposed factor. Bottom: averaged one-dimensional radius in the LCMS for pions, kaons and protons. Only three centrality bins are shown for the better readability [30]. . . . .	43
1133			
1134			
1135			
1136			
1137			
1138			
1139			
1140			
1141			
1142			
1143			
1144			
1145			
1146			
1147			
1148			
1149			